



Meso-Geometric Modeling and Failure Behavior of 2.5D Three-Harness-Twill Warp-Reinforced Woven Composites

Junhua Guo¹ · Gaofeng Zhou¹ · Huabing Wen¹ · Hongjian Zhang² · Haitao Cui² · Weidong Wen² · Chun Guo³ · Yifan Zhang⁴

Received: 16 September 2023 / Accepted: 22 November 2023 / Published online: 18 December 2023
© The Author(s), under exclusive licence to Springer Nature B.V. 2023

Abstract

A novel material, i.e. 2.5D three-harness-twill warp-reinforced woven composites (2.5D-THT-WR-WC), is proposed, which has wide engineering applications. In this work, geometrical relationships with different meso features are discussed through X-CT characterization. On this basis, six unit-cell models with different meso geometrical features are established considering different weft yarn arrangement densities M_F , and numerical simulations are carried out combined with a developed progressive damage model. Comparison with the experimental results shows that the maximum prediction errors of modulus and strength are 6.3% and 11.7%, respectively. Therefore, the developed numerical simulation model can reasonably predict the mechanical behavior of 2.5D-THT-WR-WC. Additionally, as the M_F increases, the mechanical properties in the warp and weft directions decrease and increase, respectively, owing to the inclination angle and the extrusion condition between adjacent layers of the binder yarns. This work provides a design reference for the structural application of 2.5D-THT-WR-WC, which has a significant engineering value.

Keywords 2.5D three-harness-twill warp-reinforced woven composites · Meso geometric modeling, Mechanical properties prediction · Failure mechanism analysis · Progressive damage process analysis

✉ Huabing Wen
whb@just.edu.cn

✉ Weidong Wen
gswwd@nuaa.edu.cn

¹ School of Energy and Power, Jiangsu University of Science and Technology, Zhenjiang 212100, China

² College of Energy & Power Engineering, Nanjing University of Aeronautics and Astronautics, Jiangsu 210016, People's Republic of China

³ China Ship Scientific Research Center, Wuxi 214082, China

⁴ Key Laboratory of Advanced Textile Composite Materials, Ministry of Education, Tiangong University, Tianjin 300387, China

1 Introduction

In the last decade, many fields, such as aerospace, marine navigation, and intelligent transportation, etc. [1–4], have begun to use fiber-reinforced composites instead of metals, in order to reduce the weight of the equipment, reduce energy consumption, and improve the reliability of equipment operation. In fiber-reinforced composites, 3D woven composites show the advantages of strong integrality, high designability and excellent fatigue resistance [5–9], in addition to the mechanical properties of high specific strength/stiffness that general laminated composites have. Therefore, in recent years, they have gradually received attention from various industries, such as in the application of 3D woven composites in aviation engine fan blades [10], ship propeller blades [11] and so on. Among numerous kinds of 3D woven composites, 2.5D woven composites are one of the composites with better mechanical properties, which show better fatigue resistance, damage tolerance, and overall designability [12–17] due to the fact that the binder yarns do not completely penetrate the thickness direction. Therefore, the study of mechanical properties and failure mechanism of 2.5D woven composites has been favored by scholars in recent years.

There are two typical structural forms of 2.5D woven composites, i.e. shallow curve-link-shaped (SCLS) structure [18] and shallow straight-link-shaped (SSLS) structure [19], shown in Fig. 1 (a) and (b), respectively. In the SCLS structure, a change of direction occurs at each point of intersection of the binder yarn and the weft yarn, and the binder yarn binds two layers of weft yarn in thickness. In the SSLS structure, the binder yarn needs to pass

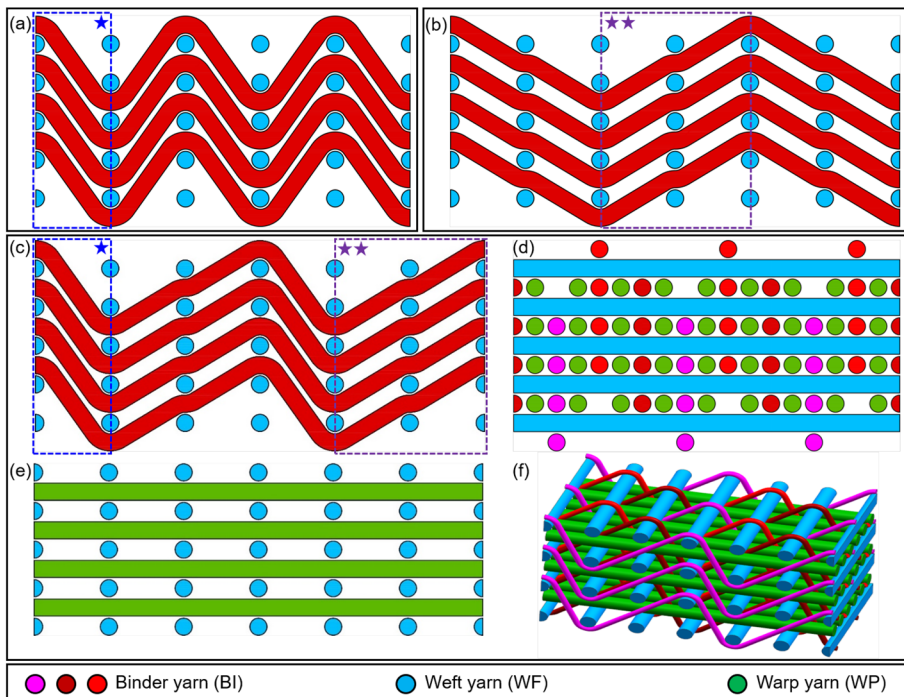


Fig. 1 Schematic of weft cross-section of 2.5D woven composites with **a** shallow curve-link-shaped and **b** straight-link-shaped structures; schematic of 2.5D-THT-WR-WC: **c** weft cross-section with binder yarn, **d** warp cross-section, **e** weft cross-section with warp yarn, and **f** 3D yarn system

through two intersections with the weft yarn before a change of direction occurs, and the binder yarn also binds two layers of weft yarn in thickness. These two structures have their own advantages in mechanical properties due to structural differences. The warp mechanical properties of the SLS structure are superior to those of the SCLS structure, while the opposite is true for the weft mechanical properties. Therefore, some scholars considered compounding the two structural forms, and the most intuitive consideration is to connect the two structural forms alternately in the yarn system so that the two structures complement each other in terms of mechanical properties. From the perspective of textile science, such a structure is in fact the classic three-harness-twill structure (see Fig. 1(c)). Furthermore, to enhance the mechanical properties of the material in the warp direction, warp yarns are added between the binder yarns to form a new material, which can be called 2.5D three-harness-twill warp-reinforced woven composites (2.5D-THT-WR-WC).

To date, few studies on 2.5D-THT-WR-WC reported in the literatures, and the vast majority of scholars investigated the unit-cell modeling methods, mechanical prediction models, and failure mechanisms of 2.5D woven composites with SCLS or SLS structures [20].

In terms of unit-cell modeling methods, there are three main approaches [21], i.e. geometric assumption approach [12, 15, 22–24], mechanics-driven approach [25–28], and reconstruction modeling approach [29–32]. Among them, the first method is currently the most widely used and also the most rapidly developed. This method is most appropriate for modeling unit cells when facing a novel yarn structure, considering the complexity and unfamiliarity of the new structure. Therefore, it is also prepared to use this method to study the meso-geometric relationship of 2.5D-THT-WR-WC in the present work.

In terms of mechanical prediction models, there are two main directions, i.e. purely theoretical formulation prediction methods and numerical simulation prediction methods. Among them, purely theoretical prediction methods, such as the selective averaging model [33], the slicing method [34], the orientation averaging method [35], and the equivalent response simulation technique [36], basically adopt the equal stress/strain assumptions, which have achieved some results in the prediction of material stiffness parameters, but it is difficult to further generalize them because they cannot effectively take the curved segments of yarns into account. Nowadays, most of the scholars choose to adopt the numerical simulation method [15, 37–40], i.e. the unit-cell finite element model combined with the progressive damage model to predict the stiffness and strength of the material. Therefore, numerical simulation method is also considered to be chosen to predict the mechanical properties of 2.5D-THT-WR-WC.

In terms of failure mechanisms, different scholars adopted different techniques to study the failure mechanisms, which mainly include SEM [8, 15, 41], X-CT [42–44] and DIC [1, 45]. However, it is difficult to filter the unique phenomena brought about by the randomness of the material by directly analyzing the material fracture only through these techniques, which in turn cannot summarize the failure mechanism with engineering value [46]. Therefore, scholars commonly adopt the combination of techniques and numerical simulations to analyze the damage process and the final fracture of the material from different perspectives, and then summarize the truthful failure mechanism. Similarly, such an approach is also considered to explore the failure mechanism of 2.5D-THT-WR-WC in this work.

In summary, it can be found that the two classical structures mentioned above have been well studied in various aspects of mechanics, but there is almost a gap in the research for 2.5D-THT-WR-WC. For this new structure, the main problems that can be foreseen from the current research on the two classical structures are: (i) differences in the alignment of the binder yarns in the SCLS and SLS structures can cause differences in the geometric characteristics of 2.5D-THT-WR-WC with different weft yarn arrangement densities, which

increases the difficulty of unit-cell geometric modeling; (ii) The effect of meso geometric differences caused by different weft yarn arrangement densities on the overall mechanical behavior of the material; (iii) would the SCLS part and the SSLS part positively complementarily or negatively counteracting in the overall mechanical properties of the material?

To address the above three key scientific issues, in this work, geometric assumptions are first made about the cross-sections of different yarns, based on which the differences in geometric characteristics under different weaving parameters are innovatively discussed and the corresponding geometric relationships are modeled. Subsequently, focusing on the geometrical differences caused by the weft yarn arrangement density on the meso structure of 2.5D-THT-WR-WC, six unit-cell models with different meso geometrical features are established, and the differences in mechanical behavior of these models are discussed by experiments and simulations. The mechanism of the influence of weft yarn arrangement density on the mechanical properties and failure mechanism of 2.5D-THT-WR-WC is summarized, which provides a theoretical basis and design reference for the engineering application of 2.5D-THT-WR-WC.

The rest of this paper can be organized as follows. In Section 2, the structural features of 2.5D-THT-WR-WC are discussed and the test methods for its specimens are given. In Section 3, the meso geometric model of 2.5D-THT-WR-WC with different weaving parameters is established. In Section 4, the progressive damage model and periodic boundary conditions are given. In Section 5, six unit-cell finite element models with different geometrical differences are developed considering different weft yarn arrangement densities. In Section 6, the results of the unit-cell models with different weft yarn arrangement densities are discussed. In Section 7, some key results are summarized.

2 Materials and Experimental Settings

2.1 Mesoscopic Structure of 2.5D-THT-WR-WC

2.5D woven composites have a variety of mesoscopic structures, among which the more typical ones are SCLS structure (see Fig. 1(a)) and SSLS structure (see Fig. 1(b)), and many of them are derived from these two types of structures, such as the 2.5D-THT-WR-WC. This structure can be regarded as a compound structure alternately combining the SCLS structure and SSLS structure, which considers the advantages of these two structures and at the same time avoids their disadvantages, so it has a wide range of application prospects.

Figure 1(c–f) presents the schematic structure of 2.5D-THT-WR-WC. From Fig. 1(d), it can be seen that in the weft direction, three rows of binder yarn form a period, and there is also a row of warp yarn between the binder yarns. As can be seen from Fig. 1(c), in 2.5D-THT-WR-WC, the direction of the binder yarns is not symmetric, specifically, the binder yarns firstly traverse downward directly through two layers and one row of weft yarns (similar to SCLS structure), and then upward through two layers and two rows of weft yarns in turn (similar to SSLS structure). It is because of the asymmetric orientation of the binder yarns that the three-harness-twill structure is also called “1/2-twill structure”. From Fig. 1(e), it can be seen that the warp yarns are directly interspersed between the two layers of weft yarns, and the orientation is relatively simple. Eventually, a yarn system can be formed as shown in Fig. 1(f).

Table 1 Woven parameters of 2.5D-THT-WR-WC used in this work [47]

Yarn type	Specifications	Arrangement density	Number of layers
Warp yarn	12 K	4 tow/cm	4
Weft yarn	12 K	6 tow/cm	6
Binder yarn	12 K	4 tow/cm	4

2.2 Material Preparation, Mesoscopic Observation

The component materials of 2.5D-THT-WR-WC used in this work are T800 carbon fiber and EC230R bismaleimide resin, and the specific weaving parameters and mechanical parameters of the component materials are listed in Tables 1 and 2, respectively. Wherein, the preforms are woven by the Key Laboratory of Advanced Textile Composite Materials of Tiangong university, and the composite molding of the preforms is completed by Aerospace Research Institute of Material & Processing Technology of China using the RTM process. After molding, the overall thickness of the material is about 3 mm and the overall fiber volume fraction is about 55%.

Figure 2 demonstrates the X-CT section of 2.5D-THT-WR-WC. As can be seen in Fig. 2(a), there is a fluctuation in the actual trend of the weft yarns, but the overall error with respect to the straight line is within a reasonable engineering range. The cross-sections of the binder yarn and warp yarn can be approximated as rectangles [2, 3, 12–19]. Analyzing the reason, from the molding mechanism, the binder yarn and the warp yarn squeeze each other, resulting in the right and left sides of the cross-section of the two yarns presenting a straight line; the weft yarn squeezes the two yarns from the thickness direction, resulting in the top and bottom sides of the two yarns also presenting a straight line. Moreover, the rectangular cross-section assumption for these two yarns not only facilitates modeling, but also effectively avoids the appearance of low-quality grids, contributing to the improvement of numerical calculation accuracy.

From Fig. 2(b), it can be seen that the binder yarn shows a wavy trend and binds the weft yarn at the top and bottom, and the cross-section of the weft yarn can be approximated as a double-sided convex lens shape. From Fig. 2(c), it can be seen that the warp yarns basically show a straight-line trend, and in the thickness direction, the warp yarn and weft yarn are arranged vertically overlapped. Moreover, the cross-sections of all yarns are assumed to be as shown in Fig. 2(d), and the data are summarized in Table 3 by measuring the calibrated locations in Fig. 2(a-c).

Table 2 Mechanical property parameters of components

Components	E_{f1} (GPa)	E_{f2} (GPa)	G_{f12} (GPa)	X_{f1} (MPa)	ν_{f12}
T800	294	19.4	15	5490	0.3
Components	E_m (GPa)	ν_m	X_m^T (MPa)	X_m^C (MPa)	S_m (MPa)
EC230R	4.04	0.35	100.6	216	66.9

E_{f1} and E_{f2} are the longitudinal and transverse moduli of carbon fibers, respectively. G_{f12} is the in-plane shear modulus of carbon fiber. X_{f1} is the longitudinal tensile strength of carbon fibers. ν_{f12} is the in-plane Poisson's ratio of carbon fibers. E_m is the elastic modulus of the resin. ν_m is the Poisson's ratio of the resin. X_m^T , X_m^C , and S_m are the tensile, compressive, and shear strengths of the resin

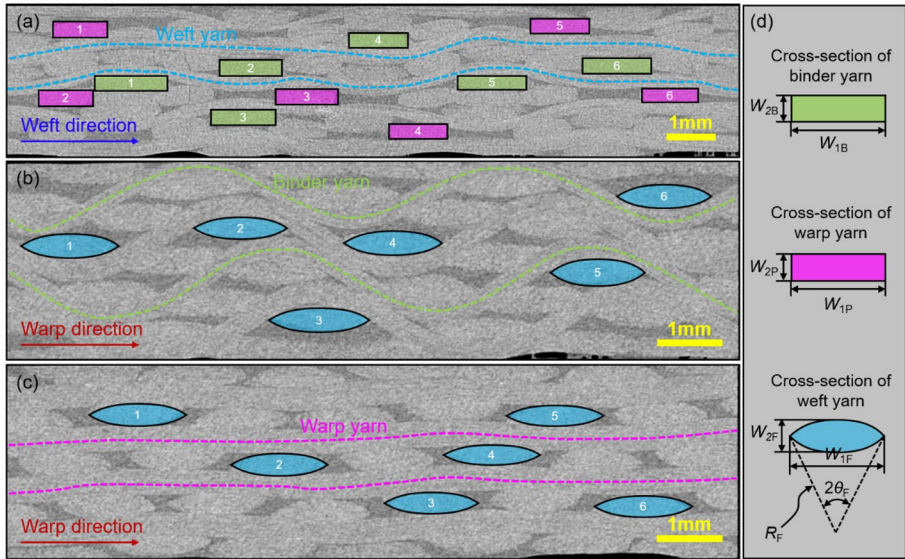


Fig. 2 Mesoscopic X-CT slices of 2.5D-THT-WR-WC used in this work: **a** warp cross-section with weft yarn, **b** weft cross-section with binder yarn, **c** weft cross-section with warp yarn, and **d** schematic of cross-section geometric parameters of different yarns

2.3 Specimens and Experimental Settings

As shown in Fig. 3(a), the specimen has a length of 230 mm, a width of 25 mm, and a thickness of 3 mm, and four reinforcing tabs are affixed to both ends with epoxy resin adhesive. The tabs have a length of 50 mm, a width of 25 mm and a thickness of 3 mm. It is worth noting that in consideration of mitigating the stress concentration effect at the clamping end due to the material difference, the tabs are made of laminated composites with the same components as the 2.5D-THT-WR-WC in this work, which is illustrated in the photograph of the specimen shown in Fig. 3(b).

Table 3 Measurements of mesoscopic geometric parameters (mm) of 2.5D-THT-WR-WC

No.	Warp cross-section with weft yarn				Weft cross-section with binder yarn		Weft cross-section with warp yarn	
	W_{1P}	W_{2P}	W_{1B}	W_{2B}	W_{1F}	W_{2F}	W_{1F}	W_{2F}
1	1.142	0.358	1.514	0.315	1.495	0.358	1.515	0.381
2	1.143	0.357	1.306	0.361	1.454	0.359	1.523	0.378
3	1.305	0.359	1.356	0.359	1.558	0.372	1.457	0.351
4	1.234	0.339	1.229	0.339	1.521	0.398	1.501	0.352
5	1.233	0.342	1.431	0.298	1.451	0.401	1.517	0.369
6	1.181	0.322	1.449	0.359	1.466	0.361	1.521	0.366
Average	1.206	0.346	1.381	0.339	1.491	0.375	1.506	0.366

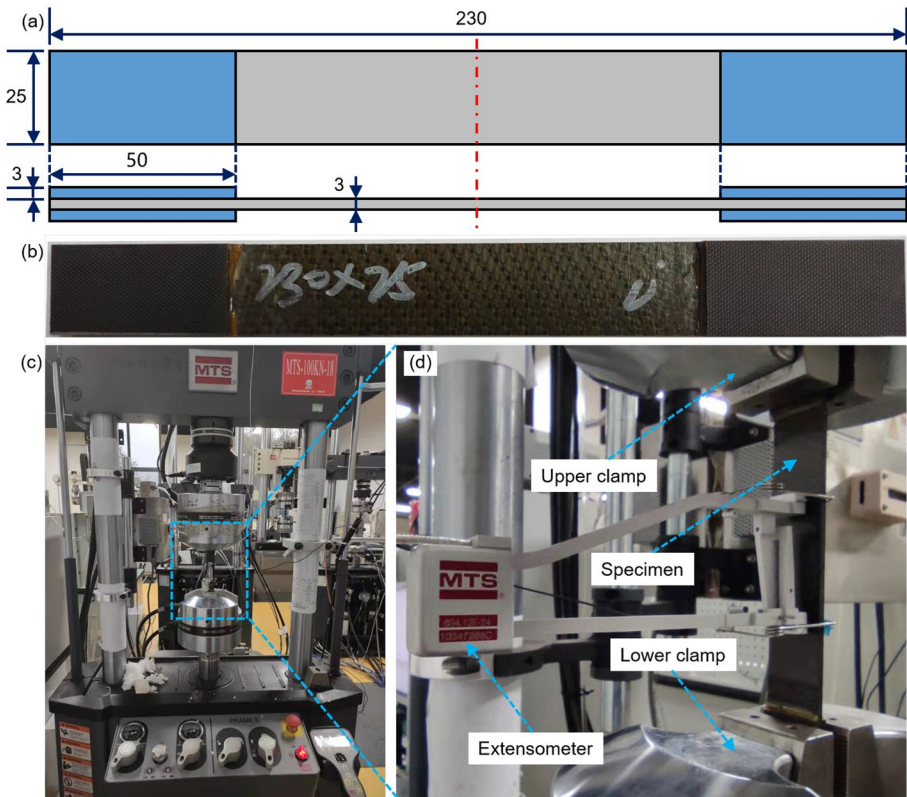


Fig. 3 Specimens and experimental settings: **a** the geometric size of the specimen, **b** photograph of the specimen, **c** tensile testing site, and **d** Enlarged view of the tensile testing site

As shown in Fig. 3(c), the static-load tensile test of the specimens is completed on the MTS370-100kN electro-hydraulic servo testing machine, the referenced experimental standard is ASTM D3039, and the ambient conditions of the experiment are dry state and room temperature (23 °C). As shown in Fig. 3(d), the extensometer used for the specimen is 634.12F-24, and the tab areas at the upper and lower ends of the specimen are clamped by the upper and lower collets of the testing machine, respectively, where the lower collet of the testing machine is kept stationary, and the upper collet of the testing machine is moved upward at the rate of 1 mm/min until the specimen breaks.

3 Meso Geometric Modeling of 2.5D-THT-WR-WC

3.1 Discussion on Several Possible Yarn Geometric Relationships

According to the schematic structure of 2.5D-THT-WR-WC shown in Fig. 1, it can be seen that the difficulty of the geometrical relationship of the structure is in determining the relationship between the binder yarn and the weft yarn. The structure of the 2.5D-THT-WR-WC can be divided into two parts during one period in the warp

direction, i.e. the SCLS part and the SSLS part. Assuming that the weft yarn cross-section is a double-sided convex lens shape, and the alignment of the binder yarn is an alternation of circular arcs and straight lines, it is not difficult to realize that a smooth transition of the binder yarn in the SSLS part is no longer possible for it to transition smoothly in the SCLS part. It is due to such constraints that there are four different cases in the geometrical relationship between these two parts.

As shown in Fig. 4, in the SCLS part, there are four positional relationships between the upper and lower binder yarns:

- (i) When the two rows of weft yarns are far away from each other (see Fig. 4(a)), the straight sections between the upper and lower binder yarns are in a state of complete separation (MN is above PQ), and the central half-angle θ_B of the curved section of the binder yarn is equal to the central half-angle θ_F of the weft yarn.
- (ii) When the two rows of weft yarns are closer to each other (see Fig. 4(b)), there exists a critical state in which the straight sections between the upper and lower layers of the binder yarns are adhered to each other (MN and PQ overlap), and the central half-angle θ_B of the curved section of the binder yarn is still equal to the central half-angle θ_F of the weft yarn.
- (iii) When the two rows of weft yarns are closer to each other (see Fig. 4(c)), the straight sections between the upper and lower layers of the binder yarns are squeezed against each other (MN and PQ overlap), and the central half-angle θ_B of the curved section of the binder yarn is smaller than the central half-angle θ_F of the weft yarn.
- (iv) When two rows of weft yarns are in contact with each other (see Fig. 4(d)), the straight sections of the upper and lower binder yarns are squeezed to a straight line, and the central half-angle of the curved section of the binder yarns is $\theta_B = 0$. This condition does not exist in practice, but is only a limiting condition.

Throughout the four conditions, it can be seen that the width of the straight section of the binder yarn is decreasing as the weft yarns continue to come closer together, which leads to an increase in the fiber volume fraction in this area.

As shown in Fig. 5, there are four positional relationships between the binder yarn and the weft yarn in the SSLS part:

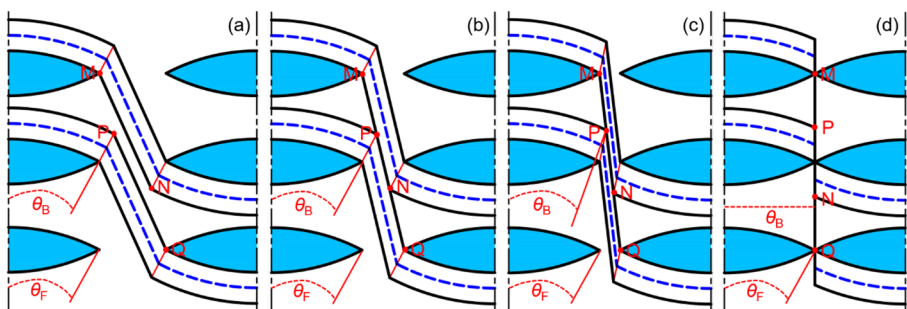


Fig. 4 Four cases of 2.5D-THT-WR-WC in the shallow curve-link-shaped part due to the different weft yarn arrangement densities: **a** complete separation, **b** critical attachment, **c** squeeze attachment, and **d** extreme attachment

- (i) When weft yarns are far from each other (see Fig. 5(a)), the binder yarns pass through the intermediate weft yarns as a straight line (BG), the straight section of which does not contact the weft yarns.
- (ii) As the distance between the weft yarns approaches (see Fig. 5(b)), the binder yarns can still pass through the intermediate weft yarns as a straight line (BG), but its straight section is just tangent to the intermediate weft yarns, with the tangent points C and F, respectively, which is a critical condition;
- (iii) When the distance between the weft yarns continues to be close (see Fig. 5(c)), the binder yarns can no longer pass through the intermediate weft yarns in a perfectly straight line, but pass through the intermediate weft yarns in the form of a circular arc (CD), a straight line (DE), and a circular arc (EF), i.e. there is a partial tangency between the binder yarns and the intermediate weft yarns.
- (iv) When the distance between the weft yarns is further approached (see Fig. 5(d)), the joining warp yarns pass through the intermediate weft yarns in a fully circular arc, i.e. circular arcs CD and DF, which is the limiting case, unlike the limiting case in the SCLS part above, which is widespread in practice.

Throughout the four conditions, it can be seen that as the weft yarns approach each other, the percentage of straight section of the binder yarn is decreasing and the percentage of curved section is increasing until the binder yarn become curved completely.

The conditions in Figs. 4 and 5 do not exist independently of each other and need to be discussed so that their respective critical and limiting conditions can be determined. In practice, the most widespread condition is the combination of Fig. 4(c) and Fig. 5(d). Actually, in the case of closely spliced yarns, when the warp yarn is higher than the binder yarn (Fig. 6(c)), the condition shown in Fig. 5(d) does not exist, whereas the above discussion makes sense only when the warp yarn is equal to or lower than the binder yarn (Fig. 4(a) and (b)).

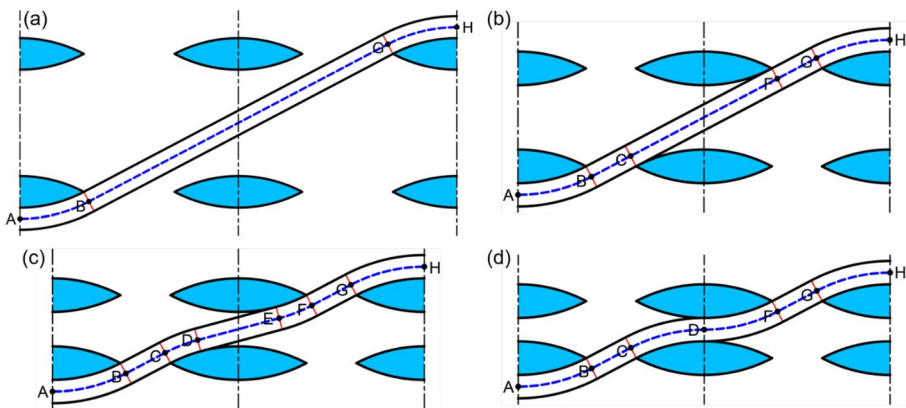


Fig. 5 Four cases of 2.5D-THT-WR-WC in the shallow straight-link-shaped part due to the different weft yarn arrangement densities: binder yarn is **a** completely separated, **b** exactly tangent, **c** partially tangent, and **d** completely tangent to the middle weft yarn

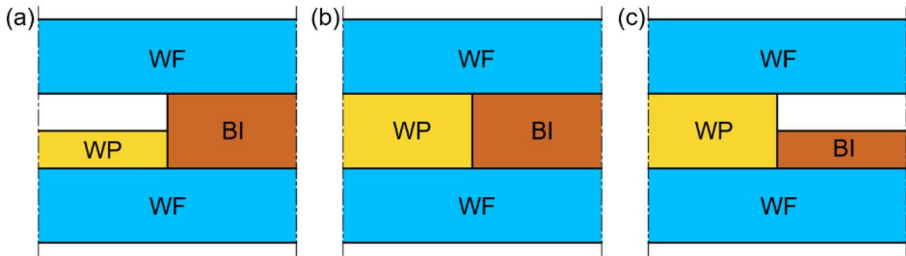


Fig. 6 Three cases of warp yarn and binder yarn in the thickness direction: the thickness of warp yarn is **a** lower than, **b** the same as, and **c** higher than that of binder yarn

3.2 Geometric Modeling of the 2.5D-THT-WR-WC

3.2.1 Geometric Relationship of the Yarn Cross-Sections

Figure 7(a-c) presents the cross-section geometrical relationships of warp yarn, binder yarn, and weft yarn, respectively. Among them, the cross-sections of the warp yarn and binder yarn are assumed to be rectangular, and the cross-section of the weft yarn is assumed to be double-sided convex lens shape. The cross-sectional areas of these three yarns need to be obtained by experimental measurements (see Table 3), so as to obtain the specific values of the width and height of different cross-sections.

As shown in Fig. 7(a) and (b), assuming that the warp yarn is closely spaced with the binder yarn, the cross-section has the following relationship for these two yarns:

$$W_{1P} = W_{1B} = \frac{10}{M_P} = \frac{10}{M_B}, \tag{1}$$

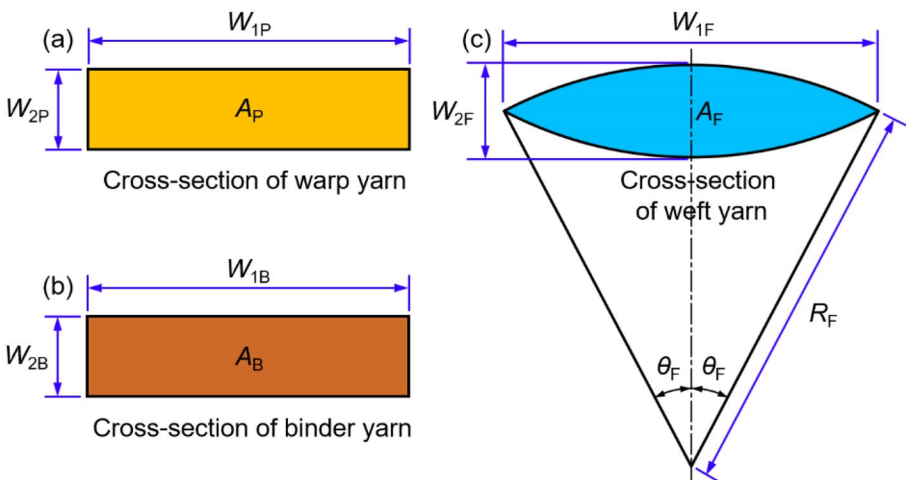


Fig. 7 Geometrical cross-sections and related parameters of **a** warp yarn, **b** binder yarn, and **c** weft yarn

$$\begin{cases} W_{2P} = A_P/W_{1P} \\ W_{2B} = A_B/W_{1B} \end{cases}, \tag{2}$$

where W_{1P} and W_{1B} are the cross-sectional widths of the warp yarn and binder yarn, respectively; W_{2P} and W_{2B} are the cross-sectional heights of the warp yarn and binder yarn, respectively; A_P and A_B are the cross-sectional areas of the warp yarn and binder yarn, respectively; M_P and M_B are the arrangement densities of the warp yarn and binder yarn, respectively.

As shown in Fig. 7(c), for the cross-section of weft yarn, following relationship exists:

$$\begin{cases} W_{1F} = R_F \sin \theta_F \\ W_{2F} = 2R_F(1 - \cos \theta_F) \\ A_F = R_F^2(2\theta_F - \sin(2\theta_F)) \end{cases}, \tag{3}$$

where W_{1F} and W_{2F} the cross-sectional width and height of the weft yarn, respectively; A_F is the cross-sectional area of the weft yarn; R_F and θ_F are the central radius and central half-angle corresponding to the weft yarn cross-section, respectively.

3.2.2 Geometric Relationships of SSSL Part

As shown in Fig. 8(a), the relationship between the transverse space D_F and the longitudinal space H_F between weft yarns in the critical tangent condition can be expressed as:

$$\begin{cases} D_F = \frac{10}{M_F} - W_{1F} \\ H_F = \frac{W_{2B}}{\cos \theta_F} + W_{1F} \tan \theta_F - W_{2F} \end{cases}. \tag{4}$$

By combining Eqs. (3) and (4), one obtains:

$$H_F \cos \theta_F + D_F \sin \theta_F = W_{2B} + \frac{10 \sin \theta_F}{M_F} + 2R_F \cos \theta_F (\cos \theta_F - 1), \tag{5}$$

where M_F is the weft yarn arrangement density.

As shown in Fig. 8(b), the transverse space D_F and longitudinal space H_F between weft yarns in the limit tangent condition can be expressed as:

$$\begin{cases} D_F = \frac{W_{2B}}{\sin \theta_F} \\ H_F = W_{2B} \end{cases}. \tag{6}$$

Then, solving Eq. (6) yields:

$$D_F = \frac{H_F}{\sin \theta_F}. \tag{7}$$

From the constraint relationships of transverse space D_F and longitudinal space H_F between weft yarns in Eqs. (5) and (7), it can be determined to which constraint relationship in Fig. 5 belongs to the geometric modeling that needs to be established. When it belongs to the completely separated condition shown in Fig. 5(a), it is relatively simple to model, while when it

belongs to the partially tangent condition shown in Fig. 5(c), it is also necessary to determine the central angle of the tangent region.

As shown in Fig. 8(c), in the partially tangent condition, setting the central half-angle occupied by the straight section of the binder yarn as θ'_F , the angle of the arc of the tangent part is $(\theta_F - \theta'_F)$, so it is sufficient to find θ'_F .

From Fig. 8(c), ΔH_{F1} and ΔH_{F2} can be represented respectively as:

$$\begin{cases} \Delta H_{F1} = \frac{1}{2} \left(H_F - \frac{W_{2B}}{\cos \theta'_F} \right) \\ \Delta H_{F2} = R_F (1 - \cos \theta'_F) \end{cases} \quad (8)$$

In addition, as can be seen from the enlarged view in Fig. 8(c):

$$\tan \theta' = \frac{\Delta H_{F1} + \Delta H_{F2}}{R_F \sin \theta'} \quad (9)$$

By combining Eqs. (8) and (9), one obtains:

$$\theta'_F = \arccos \left(\frac{2R_F + W_{2B}}{2R_F + H_F} \right) \quad (10)$$

Considering the difference in height of the warp yarn and binder yarn and assuming that yarns are spaced closely, Eq. (10) can be expressed as:

$$\theta'_F = \arccos \left(\frac{2R_F + W_{2B}}{2R_F + \max \{W_{2B}, W_{2P}\}} \right) \quad (11)$$

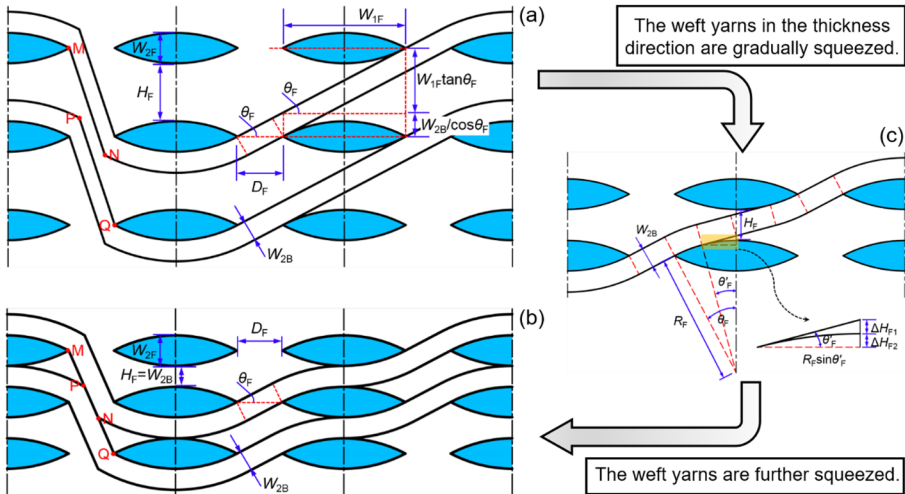


Fig. 8 Geometric relationship between the binder yarns and weft yarns at the shallow straight-link-shaped part: **a** exactly tangent, **b** partially tangent, and **c** completely tangent

3.2.3 Geometric Relationships of SCLS Part

Figure 9 illustrates the process of changing the geometric relationship between the binder yarn and weft yarn in the SCLS part. When $\angle RMQ$ is greater than $\angle SPQ$ (see Fig. 9(a)), the upper and lower binder yarns are separated; when $\angle RMQ$ is equal to $\angle SPQ$ (see Fig. 9(b)), the upper and lower binder yarns are in a critical adhesion state; when $\angle RMQ$ is less than $\angle SPQ$ (see Fig. 9(c)), the upper and lower binder yarns are squeezed together, and the central half-angle in the curved section of the binder yarn, θ''_F , is less than θ_F .

By geometrical analysis, the expression for $\angle RMQ$ and $\angle SPQ$ are obtained, i.e.

$$\begin{cases} \angle RMQ = \arctan\left(\frac{2(H_F+W_{2F})}{10/M_F-W_{1F}}\right) \\ \angle SPQ = \arctan\left(\frac{W_{2F}+H_F+W_{2B}\cos\theta_F}{10/M_F-W_{1F}-W_{2B}\sin\theta_F}\right) \end{cases} \quad (12)$$

Therefore, after determination of the geometrical relationship of the SSLS part, the geometrical relationship of the SCLS part needs to be determined firstly by the magnitude relationship between $\angle RMQ$ and $\angle SPQ$, which is simpler to model if it is a completely separated or critically adherent state. In the case of the squeezed-adherent state, it is necessary to determine the position of the point “T” in Fig. 9(c) or the central half-angle θ''_F of the binder yarn.

Determining the position of point “T” or the central half-angle θ''_F is easier with the help of analytic geometry methods, so it is necessary to establish a coordinate system for this part, as shown in Fig. 9(c). A Cartesian coordinate system is established with the center of the weft yarn cross-section as the origin, the warp direction as the x -axis direction, and the thickness direction as the y -axis direction. In this coordinate system, point “T” is the intersection of arc \widehat{TP} and line MQ , so it is sufficient to determine the equations of the arc \widehat{TP} and line MQ .

The equation of the arc \widehat{TP} is

$$x^2 + y^2 = (R_F + W_{2B})^2. \quad (13)$$

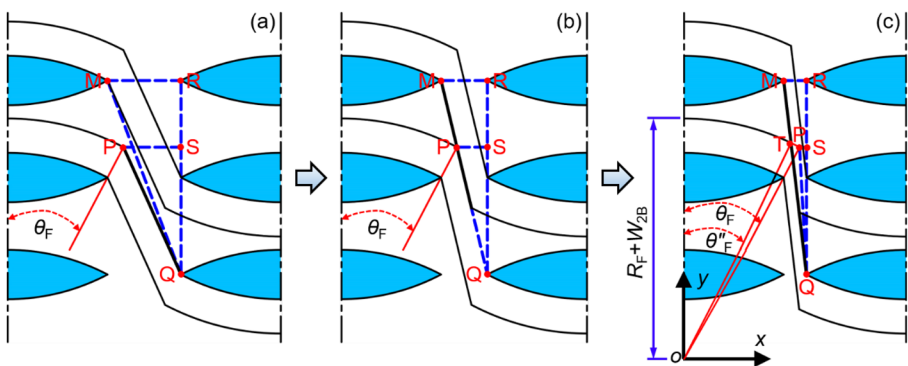


Fig. 9 Geometric relationship between the binder yarns and weft yarns at the shallow curve-link-shaped part: **a** complete separation, **b** critical attachment, and **c** extrusion attachment

In addition, the coordinates of point “M” is $\left(\frac{W_{1F}}{2}, R_F + H_F + \frac{W_{2F}}{2}\right)$, the coordinates of point “Q” is $\left(\frac{10}{M_F} - \frac{W_{1F}}{2}, R_F - H_F - \frac{3W_{2F}}{2}\right)$, so the equation of the line MQ is

$$y = \frac{2(H_F + W_{2F})}{W_{1F} - 10/M_F}x + \left(R_F - \frac{1}{2}W_{2F} - \frac{(H_F + W_{2F}) \cdot (10/M_F)}{W_{1F} - 10/M_F}\right). \tag{14}$$

By combining Eqs. (13) and (14), the coordinates of point “T” are obtained:

$$\begin{cases} x_T = \frac{\sqrt{m_B^2 n_B^2 - (1+m_B^2)(n_B^2 - (R_F + W_{2B})^2)} - m_B n_B}{(1+m_B^2)} \\ y_T = m_B x_T + n_B \\ m_B = \frac{2(H_F + W_{2F})}{W_{1F} - 10/M_F} \\ n_B = R_F - \frac{1}{2}W_{2F} - \frac{(H_F + W_{2F}) \cdot (10/M_F)}{W_{1F} - 10/M_F} \end{cases} . \tag{15}$$

The central half-angle θ''_F of the binder yarn at the squeezed-adherent state can be expressed as:

$$\theta''_F = \arctan\left(\frac{x_T}{y_T}\right). \tag{16}$$

4 Progressive Damage Model for 2.5D-THT-WR-WC

The progressive damage model is commonly used for the mechanical property prediction of composites, which consists of a set of damage onset criteria, a damage evolution model, a damage constitutive model, and a periodic boundary condition imposed on the unit-cell model.

4.1 Damage Onset Criteria

In the progressive damage process, there are mainly four damage modes of yarn, namely, yarn longitudinal tensile damage, yarn longitudinal compressive damage, yarn transverse tensile damage and yarn transverse compressive damage. For these four damage modes, different criteria are chosen in this work.

For the longitudinal tensile and compressive damage of yarns, Hashin criterion [48] is used, viz.:

$$\begin{cases} \left(\frac{\sigma_{11}}{X^T}\right)^2 + \frac{\tau_{12}^2 + \tau_{13}^2}{S_{21}^2} = 1, (\sigma_{11} \geq 0) \\ -\frac{\sigma_{11}}{X^C} = 1, (\sigma_{11} < 0) \end{cases}, \tag{17}$$

where σ_{ii} ($i=1,2,3$) is the stress of the yarn in the i -direction; τ_{ij} ($i,j=1,2,3$) is the shear stress of the yarn in the ij -direction; X^T , X^C , and S_{21} are the longitudinal tensile strength, longitudinal compressive strength, and in-plane shear strength of yarns, respectively.

For transverse tensile and compressive damage of yarns, a criterion similar to the Puck criterion but with fewer parameters is used [49], viz.:

$$\left\{ \begin{aligned} & \left[\frac{1}{Y^C \sin^2 \theta_{fp}^{YC} + Y^T} \left(\frac{2Y^C \sin^2 \theta_{fp}^{YC}}{Y^T \cos^2 \theta_{fp}^{YT}} - \frac{Y^T}{Y^C \cos^2 \theta_{fp}^{YC}} \right) \right] \sigma_n(\theta) + \\ & \left[\frac{1}{Y^C \sin^2 \theta_{fp}^{YC} + Y^T} \left(\frac{2}{Y^T \cos^2 \theta_{fp}^{YT}} + \frac{1}{Y^C \cos^2 \theta_{fp}^{YC}} \right) - \frac{1}{(Y^T \cos^2 \theta_{fp}^{YT})^2} \right] \sigma_n^2(\theta) + \\ & \left[\frac{1}{Y^C \sin^2 \theta_{fp}^{YC} + Y^T} \left(\frac{2}{Y^T \cos^2 \theta_{fp}^{YT}} + \frac{1}{Y^C \cos^2 \theta_{fp}^{YC}} \right) \right] \tau_{nt}^2(\theta) + \frac{\tau_{n1}^2(\theta)}{(S_{21} \cos \theta_{fp}^{sl})^2} = 1, (\sigma_n < 0) , \quad (18) \\ & \left[\frac{1}{Y^C \sin^2 \theta_{fp}^{YC} + Y^T} \left(\frac{2Y^C \sin^2 \theta_{fp}^{YC}}{Y^T \cos^2 \theta_{fp}^{YT}} - \frac{Y^T}{Y^C \cos^2 \theta_{fp}^{YC}} \right) \right] \sigma_n(\theta) + \\ & \left[\frac{1}{Y^C \sin^2 \theta_{fp}^{YC} + Y^T} \left(\frac{2}{Y^T \cos^2 \theta_{fp}^{YT}} + \frac{1}{Y^C \cos^2 \theta_{fp}^{YC}} \right) \right] \tau_{nt}^2(\theta) + \frac{\tau_{n1}^2(\theta)}{(S_{21} \cos \theta_{fp}^{sl})^2} = 1, (\sigma_n \geq 0) \end{aligned} \right.$$

where Y^T and Y^C are the transverse tensile and compressive strengths of the yarns, respectively; θ_{fp}^{YT} , θ_{fp}^{YC} , and θ_{fp}^{sl} is the transverse tensile, transverse compressive, and in-plane shear fracture angle of composites, for fiber-reinforced resin-matrix composites, $\theta_{fp}^{YT} = 0^\circ$, $\theta_{fp}^{YC} = 53^\circ$, and $\theta_{fp}^{sl} = 0^\circ$; $\sigma_n(\theta)$, $\tau_{nt}(\theta)$, and $\tau_{n1}(\theta)$ are defined as:

$$\begin{cases} \sigma_n(\theta) = \sigma_{22} \cos^2 \theta + \sigma_{33} \sin^2 \theta + 2\tau_{23} \sin \theta \cos \theta \\ \tau_{nt}(\theta) = -\sigma_{22} \sin \theta \cos \theta + \sigma_{33} \sin \theta \cos \theta + \tau_{23} (\cos^2 \theta - \sin^2 \theta) , \\ \tau_{n1}(\theta) = \tau_{31} \sin \theta + \tau_{21} \cos \theta \end{cases} \quad (19)$$

where θ is the potential fracture angle that needs to be iterated at $[-180^\circ, 180^\circ]$ (see Fig. 10). In fact, according to the golden section search method [50], only 3–4 searches are needed.

For the damage of pure resin matrix, an energy-based criterion is used in this work [51], viz.:

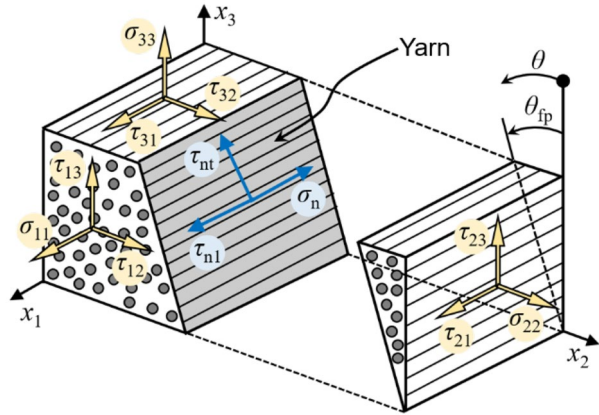
$$\left\{ \begin{aligned} & \left(\frac{1}{(X_m^T)^2} - \frac{1}{3S_m^2} \right) I_1^2 + \frac{1}{S_m^2} J_2 = 1, (I_1 \geq 0) \\ & \left(\frac{1}{\sqrt{X_m^C}} - \frac{X_m^C \sqrt{X_m^C}}{3S_m^2} \right) \sqrt{|I_1|} + \frac{1}{S_m^2} J_2 = 1, (I_1 < 0) \end{aligned} \right. , \quad (20)$$

where X_m^T , X_m^C , and S_m are the tensile, compressive and shear strengths of the pure resin matrix, respectively; $I_1 = \sigma_1 + \sigma_2 + \sigma_3$ is the first principal stress invariant of the pure resin matrix; $J_2 = [(\sigma_1 - \sigma_2)^2 + (\sigma_2 - \sigma_3)^2 + (\sigma_3 - \sigma_1)^2]/6$ is the second deviatoric stress invariant of the pure resin matrix; σ_i ($i = 1, 2, 3$) is the principal stress of the pure resin matrix in different directions.

4.2 Damage Evolution Model

When a certain damage mode occurs to an element in a component, its subsequent damage is controlled by the damage evolution model, for which the rationality of the damage evolution model is very important. One of the more widely used damage evolution models [37] is chosen in this work, viz.

Fig. 10 Schematic of yarn transverse cracking [48]



$$\left\{ \begin{aligned} d_{ik} &= \frac{X_{eq,fin}^{ik} (X_{eq}^{ik} - X_{eq,ini}^{ik})}{X_{eq}^{ik} (X_{eq,fin}^{ik} - X_{eq,ini}^{ik})}, \\ X_{eq}^{ik} &= l_{eq} \sqrt{\varepsilon_{ii}^2 + \alpha_{ik} \sum_{j=1, j \neq i}^3 \varepsilon_{ij}^2}, \end{aligned} \right. \quad (i = 1, 2, 3, m; k = T, C), \quad (21)$$

where d_{ik} is the damage factor in “ ik ” mode; X_{eq}^{ik} is the equivalent displacement, and $X_{eq,ini}^{ik}$ and $X_{eq,fin}^{ik}$ are the initial and final equivalent displacements, respectively, whose expressions are given in the literature [37]; ε_{ii} and ε_{ij} are the axial strain in the i -direction and the shear strain in the ij -direction, respectively; α_{ik} is the shear correction factor, which is defined in the literature [40]; l_{eq} is the equivalent length of the element, which is defined in the literature [37].

Therefore, the principal damage of the fiber bundle and the pure resin matrix in different directions can be expressed as:

$$D_i = \max \{d_{iT}, d_{iC}\}, \quad (i = 1, 2, 3, m). \quad (22)$$

4.3 Damage Constitutive Model

In this work, the yarn is modeled equivalently as a transverse isotropic material and the pure resin matrix is equivalent to an isotropic material, where the damage constitutive model of the transverse isotropic material can be degraded to a damage constitutive model of the isotropic material. Therefore, the damage constitutive model of the yarn and the pure resin matrix is represented here uniformly as follows:

$$\{\sigma\} = [C_d] \{\varepsilon\}, \quad (23)$$

where $\{\sigma\}$ and $\{\varepsilon\}$ denote the stress and strain of the elements, respectively; $[C_d]$ is the damage stiffness matrix, which is expressed as:

$$[C_{fb}] = \begin{bmatrix} b_{11}^2 C_{11} & b_{11} b_{22} C_{12} & b_{11} b_{33} C_{13} & 0 & 0 & 0 \\ & b_{22}^2 C_{22} & b_{22} b_{33} C_{23} & 0 & 0 & 0 \\ & & b_{33}^2 C_{33} & 0 & 0 & 0 \\ \text{sym.} & & & b_{23}^2 C_{44} & 0 & 0 \\ & & & & b_{31}^2 C_{55} & 0 \\ & & & & & b_{12}^2 C_{66} \end{bmatrix}, \tag{24}$$

where b_{ij} and C_{ij} can be respectively write as:

$$b_{ij} = \frac{2(1 - D_i)(1 - D_j)}{(1 - D_i) + (1 - D_j)}, \quad (i, j = 1, 2, 3, m), \tag{25}$$

$$\begin{cases} C_{11} = \frac{(1 - \nu_{23} \nu_{32}) E_{11}}{1 - \nu_{12} \nu_{21} - \nu_{23} \nu_{32} - \nu_{13} \nu_{31} - 2\nu_{12} \nu_{23} \nu_{31}}; C_{22} = \frac{(1 - \nu_{13} \nu_{31}) E_{22}}{1 - \nu_{12} \nu_{21} - \nu_{23} \nu_{32} - \nu_{13} \nu_{31} - 2\nu_{12} \nu_{23} \nu_{31}}; \\ C_{33} = \frac{(1 - \nu_{12} \nu_{21}) E_{33}}{1 - \nu_{12} \nu_{21} - \nu_{23} \nu_{32} - \nu_{13} \nu_{31} - 2\nu_{12} \nu_{23} \nu_{31}}; C_{23} = \frac{(\nu_{32} + \nu_{12} \nu_{31}) E_{33}}{1 - \nu_{12} \nu_{21} - \nu_{23} \nu_{32} - \nu_{13} \nu_{31} - 2\nu_{12} \nu_{23} \nu_{31}}; \\ C_{12} = C_{13} = \frac{(\nu_{21} + \nu_{23} \nu_{31}) E_{22}}{1 - \nu_{12} \nu_{21} - \nu_{23} \nu_{32} - \nu_{13} \nu_{31} - 2\nu_{12} \nu_{23} \nu_{31}}; C_{44} = G_{23}; C_{55} = G_{31}; C_{66} = G_{12}; \end{cases} \tag{26}$$

where E_{ij} , G_{ij} and ν_{ij} denote the elastic modulus, shear modulus, and Poisson’s ratio of the elements in different directions, respectively.

4.4 Periodic Boundary Conditions

To ensure the coordination of displacements and continuity of stress transfer at the unit-cell boundary, periodic boundary conditions need to be imposed on the unit-cell boundary. The displacement and force periodic boundary conditions can be expressed as [15]:

$$\begin{cases} U_i(L_j) - U_i(0) = \varepsilon_{ij} L_j, \\ \sigma_i(L_j) - \sigma_i(0) = 0, \end{cases} \quad (i, j = x, y, z), \tag{27}$$

where L_j denotes the length of the unit-cell in different directions; $U_i(L_j)$ denotes the displacement of L_j in the i -direction; $\sigma_i(L_j)$ denotes the stress of L_j in the i -direction; and ε_{ij} denotes the strain in the ij -direction.

On the basis that the unit-cell features periodic meshes, Eq. (27) can be transformed into periodic boundary conditions for the nodes in the finite element model, and the specific formula can be found in the literature [51].

5 Unit-Cell Models of 2.5D-THT-WR-WC

5.1 Geometric Models

As shown in Fig. 11, in this work, six unit-cell models are parametrically established and the basic modeling parameters are shown in Table 3. The six developed models are characterized by different weft yarn arrangement densities, M_F , and the smaller the M_F , the larger the length of the model in the warp direction; but in the thickness direction and in the weft

direction, all the models are consistent. The specific differences between the six models are described below:

- (i) When $M_F = 7 \text{ tow/cm}$ (see Fig. 11(a)), in the whole yarn system, there is not a smooth transition between the curved and straight sections of the binder yarns, the transition angle is less than θ_F , with the transition point located at the corner of the weft yarn cross-section. Additionally, there is an extrusion between the upper and lower binder yarns of the SCLS section.
- (ii) When $M_F = 6 \text{ tow/cm}$ (see Fig. 11(b)), in the SCLS section, there is not a smooth transition between the curved and straight sections of the binder yarns, the transition angle is less than θ_F , with the transition point located at the corner of the weft yarn cross-section; the upper and lower binder yarns are still extruded from each other. In the SSLS section, there is a smooth transition between the curved and straight sections of the binder yarns, with the transition point located at the corner point of the weft yarn cross-section.
- (iii) When $M_F = 5.63 \text{ tow/cm}$ (see Fig. 11(c)), in the SCLS section, there is not a smooth transition between the curved and straight sections of the binder yarns, the transition angle is equal to θ_F , with the transition point located at the corner of the weft yarn cross-section; the upper and lower binder yarns are attached to each other, but there is no compression between them. In the SSLS section, there is a smooth transition between the curved and straight sections of the binder yarns, with the transition point located on the profile line of the weft yarn cross-section.
- (iv) When $M_F = 5 \text{ tow/cm}$ (see Fig. 11(d)), in the SCLS section, there is not a smooth transition between the curved and straight sections of the binder yarns, the transition angle is equal to θ_F , with the transition point located at the corner of the weft yarn cross-section; the upper and lower binder yarns are not in contact with each other.

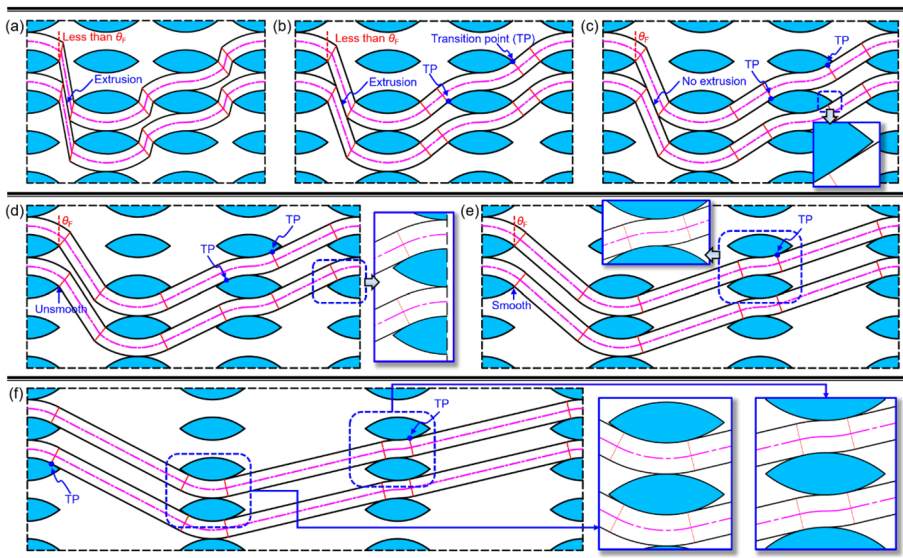


Fig. 11 Geometric relationship of yarns in weft cross-sections under different weft yarn arrangement densities: **a** 7 tow/cm, **b** 6 tow/cm, **c** 5.63 tow/cm, **d** 5 tow/cm, **e** 4 tow/cm, and **f** 3 tow/cm

In the SCLS section, there is a smooth transition between the curved and straight sections of the binder yarns, with the transition point located on the profile line of the weft yarn cross-section.

- (v) When $M_F = 4\text{tow/cm}$ (see Fig. 11(e)), in the SCLS section, there is a smooth transition between the curved and straight sections of the binder yarns, the transition angle is equal to θ_F , with the transition point located at the corner of the weft yarn cross-section; the upper and lower binder yarns are not in contact with each other. In the SCLS section, there is a smooth transition between the curved and straight sections of the binder yarns, with the transition point located on the profile line of the weft yarn cross-section.
- (vi) When $M_F = 3\text{tow/cm}$ (see Fig. 11(f)), in the SCLS section, there is a smooth transition between the curved and straight sections of the binder yarns, the transition angle is equal to θ_F , with the transition point located on the profile line of the weft yarn cross-section; the upper and lower binder yarns are not in contact with each other. In the SCLS section, there is a smooth transition between the curved and straight sections of the binder yarns, with the transition point located on the profile line of the weft yarn cross-section.

5.2 Finite Element Models

To explore the mechanical behavior of 2.5D-THT-WR-WC with different M_F , corresponding finite element models are established for each of the six established unit-cell geometrical models, as shown in Fig. 12. The meshes of all unit-cell finite element models in all three directions (x , y , z) exhibit periodicity, i.e. the other two coordinates of the two nodes on the opposite side are the same in a certain direction, thus guaranteeing the imposition of periodic boundary conditions. Considering the strong interfacial properties of carbon-fiber-reinforced resin-matrix composites, the finite element models of different components are connected by means of common nodes. The element type of all meshes is SOLID185 in ANSYS software, which is a hexahedral eight-node element that can also be degenerated into trigonal six-node element, pyramidal five-node element,

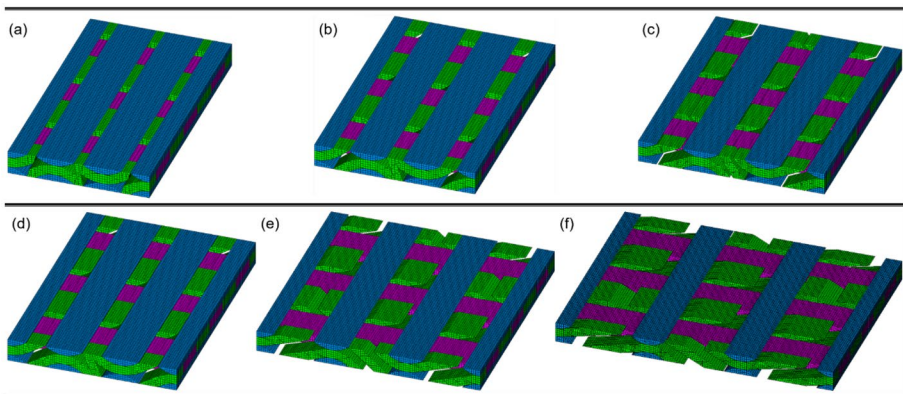


Fig. 12 Finite element models of unit-cells (removing the mesh of pure matrix) of 2.5D-THT-WR-WC with different weft yarn arrangement densities: **a** 7 tow/cm, **b** 6 tow/cm, **c** 5.63 tow/cm, **d** 5 tow/cm, **e** 4 tow/cm, and **f** 3 tow/cm

and tetrahedral four-node element, and is commonly used to simulate the deformation behavior of solids.

Table 4 presents statistics on the elemental counts of all unit-cell models and their components. Obviously, as the M_F decreases, the larger the length of the unit-cell finite element model in warp direction, the larger the number of elements, and the longer the computation time required. The finite element models contain only hexahedral eight-node elements and trigonal hexahedral elements, in which the hexahedral eight-node elements account for the majority of them, with a ratio of more than 70%, in other words, the unit-cell finite element models developed in this work are of high quality. In addition, the element size of all unit-cell finite element models is set to 0.06 mm, and from the sensitivity validation of the mesh density done in the literature [15], it can be seen that when the element size is 0.06 mm, the maximum relative error is only 2.8%, and more accurate calculation results can be obtained.

5.3 Yarn Properties with Different fiber Volume Fractions in Unit-Cell Models

In different unit-cell models, the fiber volume fraction of different yarns is different, and even the fiber volume fraction of yarns in different regions is variable due to the internal extrusion. Eq. (28) gives the calculation of fiber volume fraction of yarns in different regions:

$$V_f^{\text{yarn}} = \frac{T_c}{1000\rho_f A^{\text{yarn}}} \times 100\%, \quad (28)$$

where V_f^{yarn} is the fiber volume fraction of yarn; T_c is the linear density of the fiber, and the linear density of T800 carbon fiber is 445 g/1000 m; ρ_f is the density of the fiber, and the density of T800 carbon fiber is 1.8 g/cm³; A^{yarn} is the cross-sectional area of different yarns in different regions.

Furthermore, the stiffness and strength of the yarn in different regions also differ due to the difference in the fiber volume fraction of the yarn in different regions. The specific formula for the mechanical properties of the yarn is given in Table 5, and according to which the mechanical properties of the yarn in different regions can be calculated.

Table 4 Statistics on the element number of different unit-cell finite element models

M_F	Pure matrix	Warp yarn	Binder yarn	Weft yarn	Total
3	84672	43488	45792	20736	194688
4	56160	30816	33408	20736	141120
5	49344	28512	33312	23040	134208
5.63	32640	22464	26688	21312	103104
6	28224	19584	23616	20736	92160
7	23232	17856	21696	20736	83520

Table 5 Mechanical properties of yarn [15]

Mechanical properties	Calculation formula
Longitudinal modulus	$E_{11}^{yarn} = V_f E_{f11} + (1 - V_f) E_m$
Transverse modulus	$E_{22}^{yarn} = (E_m E_{f22} (V_f + 0.661(1 - V_f))) / (E_m V_f + 0.661 E_{f22} (1 - V_f))$
In-plane off-axis modulus	$E_{45}^{yarn} = \frac{0.938 E_m E_{f22}}{E_m V_f + E_{f22} (1 - V_f)} + 0.062 (V_f E_{f11} + (1 - V_f) E_m)$
Longitudinal strength	$X_{1k}^{yarn} = 0.736 (V_f X_{f11k} + (1 - V_f) X_{mk}) \quad (k = 'T', 'C')$
Transverse strength	$X_{2k}^{yarn} = \left 673.82 \left(1 - \left(3.05 \sqrt{V_f} - 2.322 V_f \right) \right) \right \cdot \left(1 - \frac{E_m}{E_{f22}} \right) X_{mk} \quad (k = 'T', 'C')$
In-plane shear strength	$S_{12}^{yarn} = 107.483 (1 + 0.942 V_f)$
In-plane Poisson's ratio	$\nu_{12}^{yarn} = V_f \nu_{f12} + (1 - V_f) \nu_m$
In-plane Poisson's ratio	$\nu_{21}^{yarn} = E_{22}^{yarn} \nu_{12}^{yarn} / E_{11}^{yarn}$
In-plane shear modulus	$G_{12}^{yarn} = \left(\frac{4}{E_{45}^{yarn}} - \frac{1}{E_{11}^{yarn}} - \frac{1}{E_{22}^{yarn}} + \frac{2\nu_{21}^{yarn}}{E_{11}^{yarn}} \right)^{-1}$

6 Results and Discussions

6.1 Mechanical Properties Prediction and Validation

Table 6 provides a comparison of the experimental data with predicted values for the modulus and strength of 2.5D-THT-WR-WC with $M_F = 6$ tow/cm. In general, the maximum error in modulus is 6.3%, which occurs in the weft modulus prediction, and the maximum error in strength is 11.7%, which occurs in the warp strength prediction. Therefore, the established unit-cell model combined with the developed progressive damage model in this work can reasonably predict the mechanical properties of 2.5D-THT-WR-WC.

Figure 13 shows the trend of modulus and strength of 2.5D-THT-WR-WC with different M_F . It can be seen that both the modulus and strength in warp direction decrease with the increase of M_F , while both properties in weft direction increase with the increase of M_F , and the variation magnitude of both properties in warp direction is significantly smaller than that in weft direction. The reason for this is that the yarn cross-section and thickness are kept constant for all unit-cell models in this work, so that as the M_F increases, the volume percentage of the warp yarn remains constant, the volume percentage and the inclination angle of the binder yarn increase, and the volume percentage of the weft yarn increases. Under warp-loading, the warp yarn plays the main load-bearing role, and the binder yarn plays the secondary load-bearing role. In the case of the constant volume percentage of the warp yarn, the inclination angle of the binder yarn increases with the increase of the M_F , leading to the decrease of the warp-load that it can share, and then leads to the decrease of the mechanical properties in warp direction. Under weft-loading, the weft yarn plays the main load-bearing role, and the weft yarn volume percentage increases with the increase of M_F , thus the mechanical properties in weft direction are improved.

6.2 Initial Stress Field Analysis

Figures 14 and 15 show the initial first principal stress clouds (S11) under warp-loading and weft-loading, respectively, both loaded at a strain of 0.1%. Overall, under warp-loading,

Table 6 Experimental verification of the mechanical properties of 2.5D-THT-WR-WC with $M_f = 6\text{tow/cm}$

Loading direction	Modulus (GPa)			Strength (MPa)										
	Experiment			Predicted		Error		Experiment			Predicted		Error	
	No.1	No.2	No.3	Average			No.1	No.2	No.3	Average				
Warp	55.5	56.8	61.1	57.8	60.2	4.2%	652.7	682.1	710.3	681.7	761.6	11.7%		
Weft	61.3	63.4	59.7	61.5	57.6	6.3%	804	854	831	829.7	898.1	8.2%		

The experimental data under weft-loading are from the literature [52]

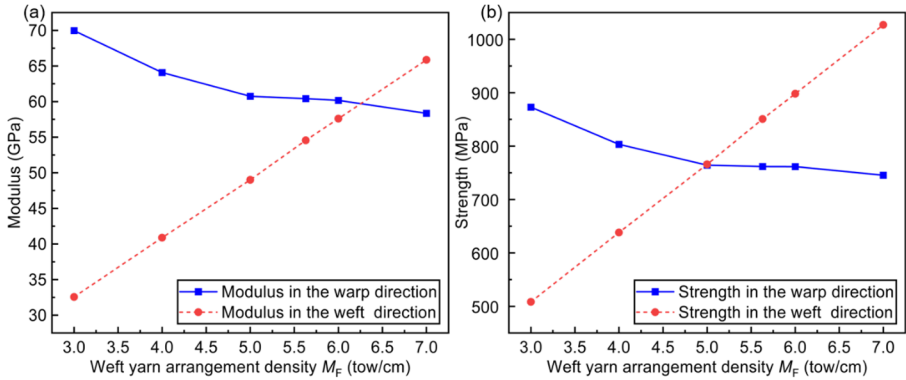


Fig. 13 Variation of the mechanical properties of 2.5D-THT-WR-WC with different weft yarn arrangement densities: **a** modulus and **b** strength

the stress of the warp yarn is the largest, followed by the binder yarn, and the stresses of the weft yarn and the matrix are similar; under weft-loading, the stress of the weft yarn is the largest, and the stresses of the other components are similar. Moreover, the stresses of

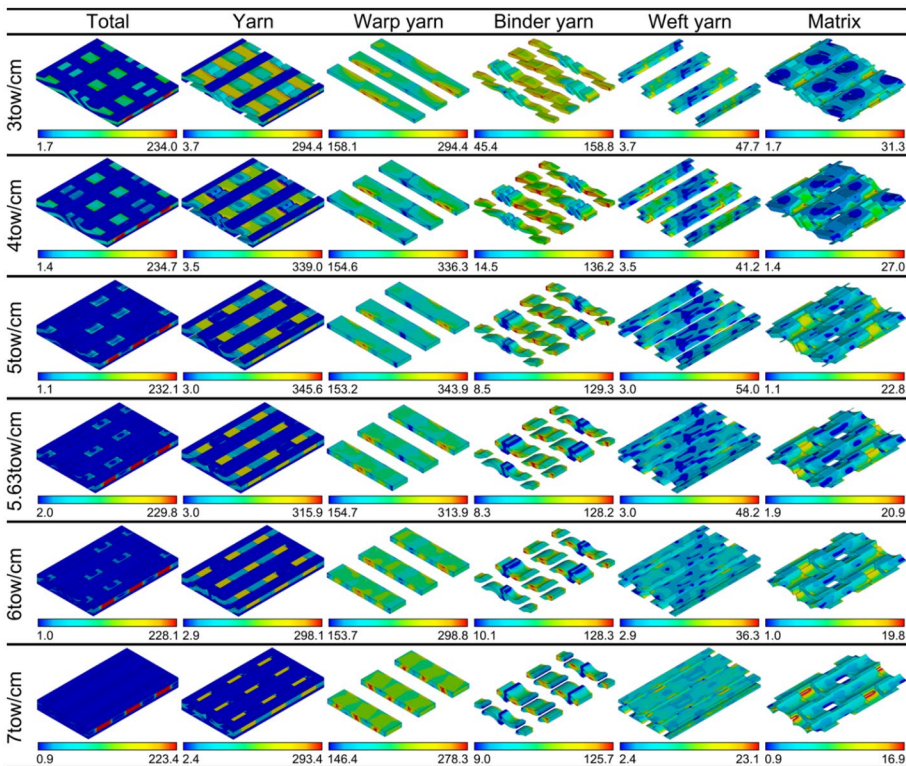


Fig. 14 First principal stress nephograms for different unit-cell models with initial warp-loading strain of 0.1%

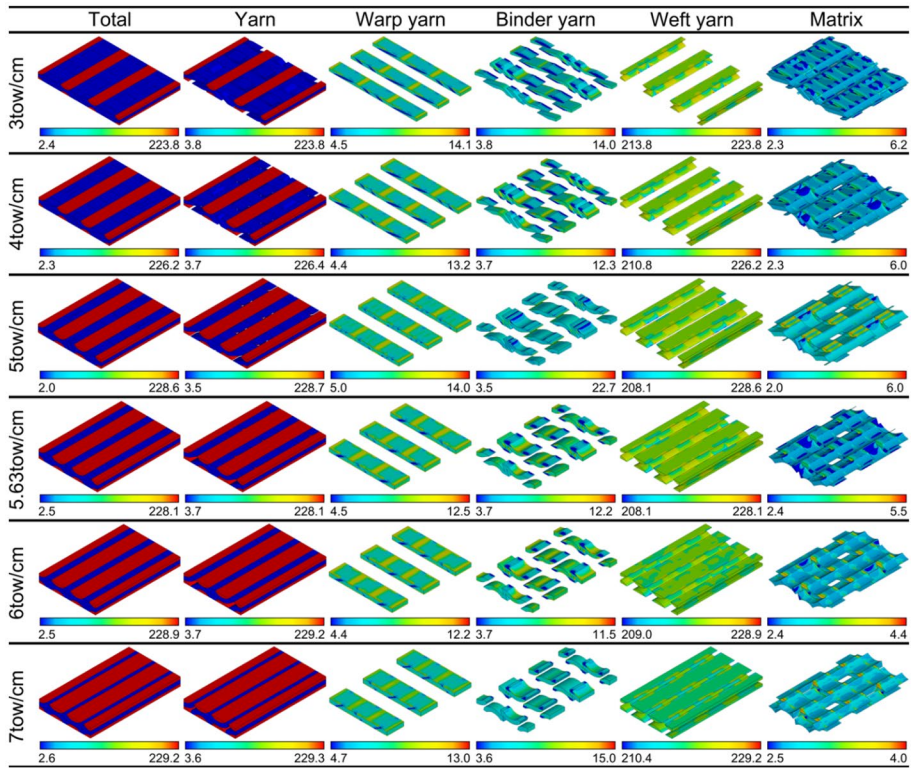


Fig. 15 First principal stress nephograms for different unit-cell models with initial weft-loading strain of 0.1%

unit-cell can be characterized by periodicity under both warp-loading and weft-loading, indicating that the periodic boundary conditions imposed in this work are effective.

From Fig. 14, it can be seen that under warp-loading, the stresses in the whole unit cell, the binder yarn, and the pure matrix show a decreasing trend with the increase of M_F , which is due to the increase of the inclination angle of the binder yarn. However, the stresses in the yarn system, warp yarn, and weft yarn show a tendency to increase first and then decrease. Investigate its reason, the point of maximum stress occurs at the transition point where the binder yarn contacts the warp and weft yarn, which is due to the fact that the binder yarn is gradually stretched out under warp-loading, and shear stresses are formed on the warp and weft yarn. When the M_F is smaller, the adjacent layers of the binder yarns are farther apart, and the interference effect cannot occur at the two stress concentration sites; when the M_F is greater, the adjacent layers of the binder yarns are squeezed each other, and there is only one stress concentration site; When $M_F = 5\text{tow/cm}$, the two stress concentration sites are close to each other and the interference effect of stress concentration occurs, causing the stress concentration effect to be more significant.

From Fig. 15, it can be seen that under weft-loading, the stress of the whole unit-cell as well as each component does not change significantly with the increase of M_F , and the stress of the weft yarn is significantly higher than that of other components. This is due to the fact that under weft-loading, the weft yarn is in the longitudinal loading state, the other

yarns are in the transverse loading state. And there is almost no shear stress between the binder yarn and the other yarns, which is similar to the axial-loading of the fiber bundle, and the distribution of the overall stress field is relatively simple.

6.3 Stress-Strain Response Analysis

Figure 16 presents the experimental validation of the stress-strain response of 2.5D-THT-WR-WC under warp-loading and weft-loading, as well as the comparison of the stress-strain curves with different M_F .

From Fig. 16(a), it can be seen that the experimental curves are slightly lower than the predicted curves under warp-loading, which satisfies the accuracy requirement within the engineering error. When the loading strain is about 0.7%, the curve begins to show nonlinearity, indicating that damage is beginning to occur within the material, when damage is generally dominated by matrix cracking and transverse damage to the yarns [12]. When the loading strain is about 1.4%, the material begins to lose its load-bearing capacity, indicating that yarn breaks are occurring within the material, especially the warp yarn.

From Fig. 16(b), it can be seen that the stress-strain curve decreases with the increase of M_F under warp-loading. When M_F is smaller, the stress-strain curve changes with M_F

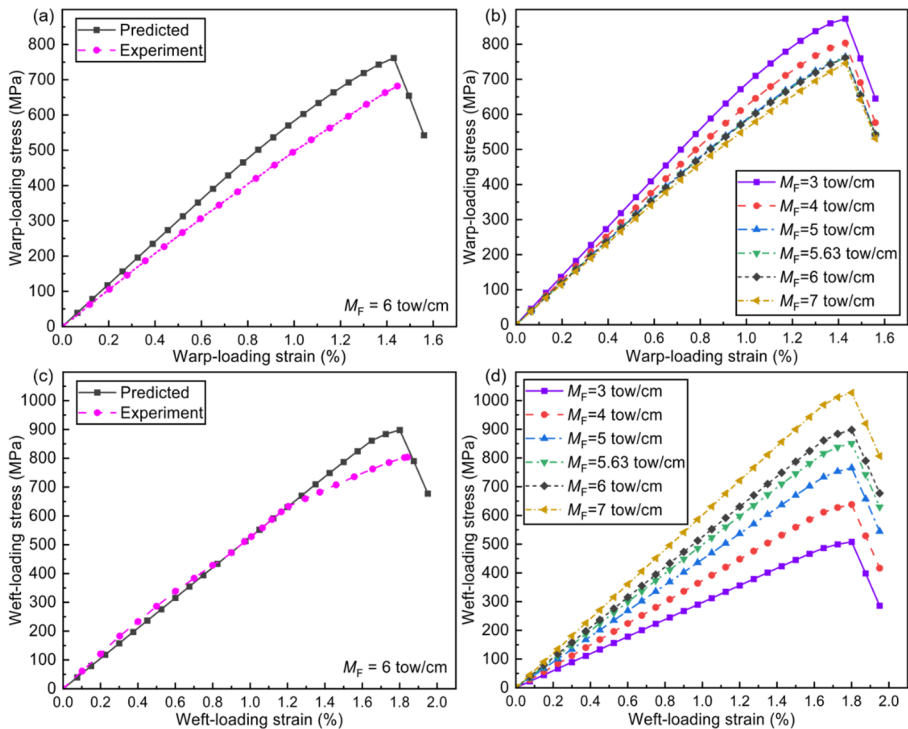


Fig. 16 Stress-strain response of 2.5D-THT-WR-WC: **a** variation of the warp-loading stress-strain curves, **b** warp-loading stress-strain curves with different weft yarn arrangement densities, **c** variation of the weft-loading stress-strain curves, and **d** weft-loading stress-strain curves with different weft yarn arrangement densities

in a larger magnitude, and the overall curve nonlinearity is weaker; when M_F is larger, the stress-strain curve changes with M_F in a smaller magnitude, and the curve nonlinearity is stronger. Investigate its reason, when the M_F is smaller, the inclination angle of the binder yarn is smaller, which tends to be linear, and the internal damage mode is relatively simple and tends to be characterized by elastic-brittle fracture during the loading process. Conversely, when M_F is larger, the inclination angle of the binder yarn is larger, and the shear effect between the binder yarn and other components is more significant during the loading process, and the internal damage mode is more complicated, which tends to be elastic-plastic fracture characteristics.

From Fig. 16(c), it can be seen that under weft-loading, the experimental curve is in good agreement with the predicted curve. When the loading strain is about 1.6%, the slope of the curve decreases and fatal damage begins to appear inside the material, when the damage is generally manifested as localized fracture of the weft yarn. When the loading strain is about 1.8%, the material begins to lose the load-bearing capacity, indicating that the weft yarns are completely fractured.

From Fig. 16(d), it can be seen that under weft-loading, the stress-strain curves increase with the increase of M_F , and the nonlinearities are basically the same between different curves except for the difference of slopes. The reason for this is that under weft-loading, the overall fiber volume fraction increases [54, 55], especially the volume percentage of weft yarn improves, with the increase of M_F , thus making the stiffness and strength in weft direction increase. Besides, there is no shear effect of the binder yarn with other components inside the material, and the damage mode is relatively simple, which is similar to the 0° loading of unidirectional composites, showing significant brittle fracture characteristics. And the brittle fracture characteristics are more significant under weft-loading than those under warp-loading.

6.4 Failure Mechanism and Ultimate Damage Nephograms Analysis

6.4.1 Ultimate Damage under Warp-Loading

Figure 17 shows the comparison between the experimental fracture and the ultimate damage nephograms under warp-loading. Therein, Fig. 17(a-d) presents the experimental fracture at different scales, and Fig. 17(e-k) presents the final damage nephograms of the unit-cell obtained by simulation.

From Fig. 17(a-d), the following characteristics can be observed:

- (i) Macroscopically, the overall fracture is relatively flat, with many warp yarns and binder yarns pulling out (see Fig. 17(a)).
- (ii) Mesoscopically, the damage mode mainly consists of longitudinal breakage and transverse cracking of warp and binder yarns, with significant weft yarns debonding, and matrix fragments attached to the debonded weft yarns (see Fig. 17(b-c)).
- (iii) Microscopically, the fibers on the fracture of the binder yarns showed an exploded shape with matrix fragments attached (see Fig. 17(d)).

As can be seen from Fig. 17(e-k), in general, the damage locations and modes shown in the ultimate damage nephograms of each component can be consistent with the actual fracture to a certain extent, which is mainly reflected in the following aspects:

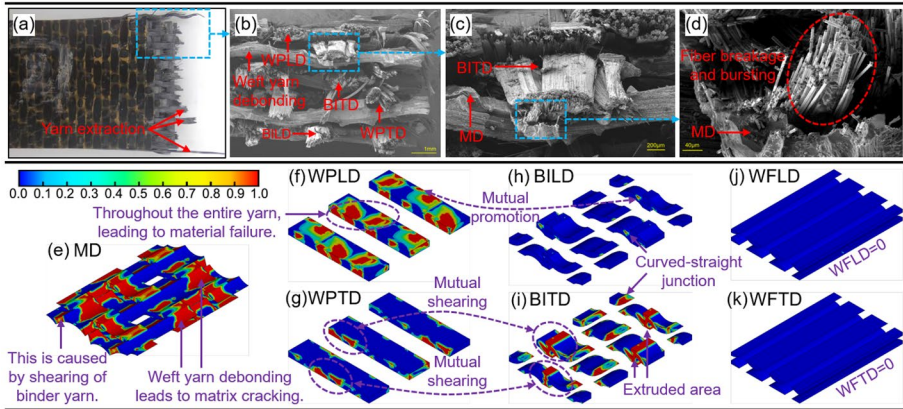


Fig. 17 Comparison of experimental fracture with ultimate damage nephograms under warp-loading, where **a–d** are the experimental results: **a** Macroscopic fracture, **b** and **c** mesoscopic fracture, and **(d)** microscopic fracture; **e–k** are the simulation results: **e** matrix damage (MD), **f** warp yarn longitudinal damage (WPLD), **g** warp yarn transverse damage (WPTD), **h** binder yarn longitudinal damage (BILD), **i** binder yarn transverse damage (BITD), **j** weft yarn longitudinal damage (WFLD), and **k** weft yarn transverse damage (WFTD)

- (i) As shown in Fig. 17(e), the matrix damage (MD) is mainly divided into two parts, the first part is mainly the matrix between adjacent layers of the binder yarns, which is mainly due to their shearing, and the second part is mainly the matrix around the weft yarns, which is mainly due to the weft yarns debonding. Both of parts can correspond to the actual fracture.
- (ii) As shown in Fig. 17(f–g), warp yarns longitudinal damage (WPLD) almost extends laterally through each warp yarn, while warp yarns transverse damage (WPTD) occurs mainly at their edges. Observing the warp yarn fracture in Fig. 17(b), it can be found that the warp yarn fracture is relatively flat, and only their edges are cracked, while their inner part is almost not cracked. Therefore, the simulated damage pattern is consistent with the actual fracture.
- (iii) As shown in Fig. 17(h–i), the binder yarns longitudinal damage (BILD) mainly occurs at the edges of their curved-straight junction area, while the binder yarns transverse damage (BITD) can be divided into two parts, the first one is the squeezing part of their adjacent layers, and the second part is their curved-straight junction area. Among them, the first part of the BITD is mainly caused by their straightening effect during the tensile process, which leads to the mutual separation between their adjacent layers; the second part of the BITD is mainly caused by the squeezing and shearing effect between the binder yarns and other components. Observing the fracture of the binder yarns in Fig. 17(c), it can be noticed that they have very severe transverse cracking, which is consistent with the BITD damage cloud. It is worth noting that the pull-out phenomenon of the binder yarn is formed after the warp yarn breaks and the tester rips it off at the final stage, and is not a break formed during the normal loading process, as evidenced by the fact that the fiber monofilaments show a blown-up shape in Fig. 17(d).
- (iv) As shown in Fig. 17(j–k), the two modes of weft yarns longitudinal damage (WFLD) and weft yarns transverse damage (WFTD) almost do not occur. Observation of

Fig. 17(b-c) shows that the weft yarns in the fracture are mainly debonded, and almost no breakage or cracking occurs, which is consistent with the simulation results.

Therefore, the established unit-cell finite element model combined with the developed progressive damage model can reasonably simulate the failure mode of 2.5D-THT-WR-WC under warp-loading.

Figure 18 illustrates the comparison of the ultimate damage patterns of each component with different M_F under warp-loading. As the M_F increases, the damage of each component exhibits the following characteristics:

- (i) The overall degree of MD decreases, complete MD (C_MD), i.e. $MD = 1$, changes from contiguous to segmented areas, the overall damage area decreases, and the area of incomplete MD, i.e. $MD < 1$, increases, indicating a decrease in the damage degree of weft yarns debonding.
- (ii) WPLD gradually changes from inclined through the warp yarns to lateral through them, and the damage area becomes more concentrated; while WPTD gradually changes from lateral through the warp yarns to occur only at their edge, with fewer damage area and lower damage degree.
- (iii) BILD gradually changes from lateral through the binder yarns to occurring only at their edges, with fewer damage area and lower damage degree. Conversely, BITD

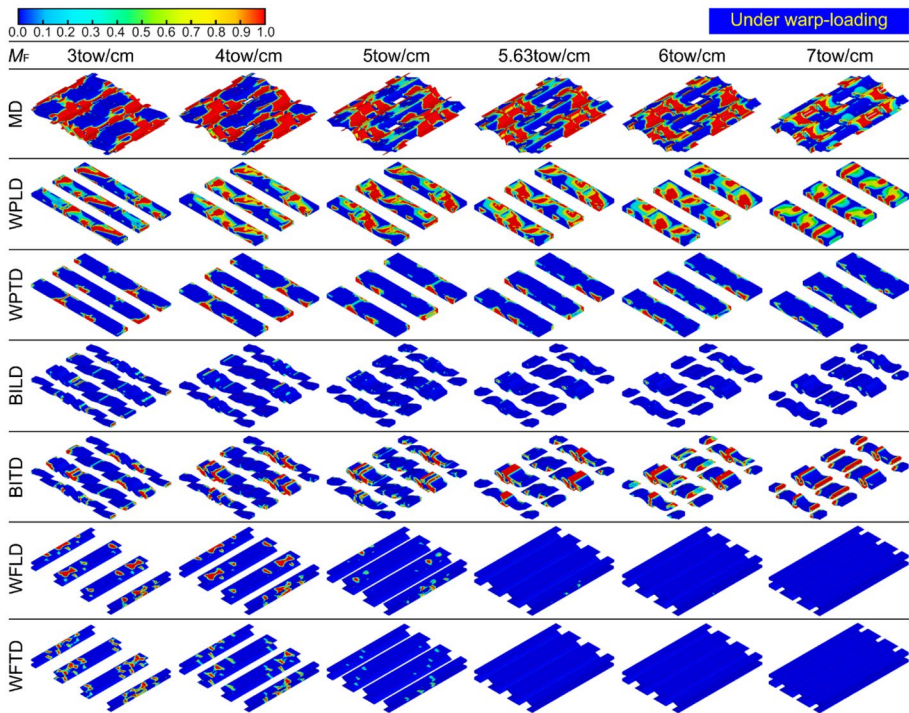


Fig. 18 Comparison of ultimate damage nephograms of various components with different weft yarn arrangement densities under warp-loading

increases from occurring only at the edge of the binder yarns to lateral through the entire binder yarns, with more damage area and higher damage degree.

- (iv) Both WFLD and WFTD gradually change from lateral through weft yarns to only sporadic damage and then to almost no damage.

The reason for the above characteristics is that, as M_F increases, the inclination angle of the binder yarn increases, the percentage of load shared by binder yarn and warp yarn decreases and increases under warp-loading, respectively, resulting in a more significant brittle fracture features of the warp yarn, i.e. the damage area is reduced and concentrated. Further, due to the decrease in the percentage of load shared by binder yarns, the force between the binder yarns, matrix, and weft yarns decreases, resulting in a decrease in the overall damage degree of the matrix and weft yarns. In the literatures [56–58], the authors investigated the effect of binder yarn binding pattern on the overall material mechanical properties and gave similar conclusions, which justify the findings of this work.

6.4.2 Ultimate Damage under Weft-Loading

Figure 19 demonstrates the comparison of experimental fracture and final damage clouds under weft-loading. Therein, Fig. 19(a-d) gives the experimental fracture at different scales and Fig. 19(e-k) gives the final damage clouds of the unit-cell obtained by simulation.

From Fig. 19(a-d), the following features can be observed:

- (i) Macroscopically, the fracture (see Fig. 19(a)) shows significant warp yarn debonding and weft yarn pull-out, the overall fracture is not flat enough, and there is a significant zoning phenomenon, i.e. one part has warp yarn debonding as the main failure pattern, and the other part has weft yarn pull-out as the main failure pattern.
- (ii) Mesoscopically, significant transverse cracking is observed in the warp yarns and the binder yarns, and some fragmented matrix is adhered to the warp yarns near the fractures (see Fig. 19(b)).

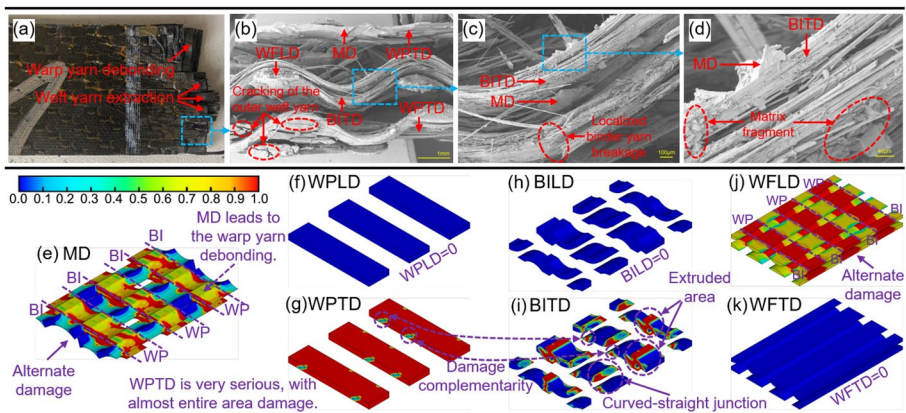


Fig. 19 Comparison of experimental fracture with ultimate damage nephograms under weft-loading: **a** Macroscopic fracture, **b** and **c** mesoscopic fracture, and **d** microscopic fracture; **e** MD, **f** WPLD, **g** WPTD, **h** BILD, **i** BITD, **j** WFLD, and **k** WFTD

- (iii) Mesoscopically, significant longitudinal breakage of the weft yarns occurs, and transverse cracking is present at the fractures of the external weft yarns but not the internal weft yarns, due to the internal weft yarns being constrained by the surrounding components (see Fig. 19(b)).
- (iv) A few longitudinal breaks exist on the transversely cracked knotting yarn (see Fig. 19(c)), which is caused by the stress concentration inside the binder yarn when the binder yarn is transversely cracked which cuts off the fibers locally.
- (v) Microscopically, there are more matrix fragments adhering to the fracture of the binder yarns (see Fig. 19(d)), indicating a more significant brittle fracture of the material under weft-loading.

As can be seen from Fig. 19(e-k), the damage locations and modes shown in the ultimate damage nephograms of each component can be consistent with the actual fracture to a certain extent generally, which is mainly reflected in the following aspects:

- (i) As shown in Fig. 19(e), the MD exhibits the phenomenon of alternate damage, i.e. the matrix alongside the binder yarns is lightly damaged ($MD < 0.4$), while the matrix alongside the warp yarns is severely damaged ($MD > 0.8$). Observation of the breaks in Fig. 19(b) shows that there are blocks of matrix adhering to the warp yarn breaks, whereas only matrix fragments are present on the binder yarns, thus explaining the reasonableness of the simulation. The reason for this is that the binder yarns and weft yarns are bound, and the strain energy of the binder yarns can be effectively transferred to the weft yarns, which ensures that the degree of BITD is much smaller than that of WPTD. Accordingly, the damage to the matrix, which is alongside the knotting yarns, is weakened.
- (ii) As shown in Fig. 19(f-g), WPLD almost does not occur, while WPTD almost completely covers the entire warp yarns, only a small area at their edge is undamaged. Observation of the warp yarn breaks in Fig. 19(b) shows that transverse cracking occurs almost as a whole, but its longitudinal breakage is almost not observed.
- (iii) As shown in Fig. 19(h-i), similar to WPLD, BILD almost does not occur, but BITD is very pronounced in the extruded region of the adjacent layers of binder yarns and in the curved-straight junction area, which can be easily observed from the test fracture in Fig. 19(b-c). The reason for this is that the binder yarns and the weft yarns are bound to each other so that the binder yarns are not damaged due to the restriction of the weft yarns in the spatial position.
- (iv) As shown in Fig. 19(j-k), the WFLD is similar to the MD, with a significant alternating damage phenomenon, for reasons similar to those in (i) above, which will not be repeated here. In addition, WFTD almost does not occur, which is more similar to the internal weft breaks shown in Fig. 19(b and c), further illustrating the reasonableness of the simulation.

Consequently, the established unit-cell finite element model combined with the developed progressive damage model can reasonably simulate the failure mode of 2.5D-THT-WR-WC under weft-loading.

Figure 20 shows the comparison of the ultimate damage modes of each component with different M_F under weft-loading. It should be noted that the three damage modes, WPLD, BILD, and WFTD, do not appear for all unit-cells under weft-loading, which

are not shown here. As the M_F increases, the overall fiber volume fraction improves, the damage of each component exhibits the following characteristics:

- (i) The general degree of MD increases, and the complete MD (C_MD) gradually shifts from the plane where the center axis of the warp yarns is located to the plane where their two sides are located, indicating an increase in the degree of the warp yarns debonding.
- (ii) The overall degree of WPTD is increased, mainly reflecting the reduction of undamaged regions, as illustrated by the regional shift in C_MD described above.
- (iii) The overall degree of BITD is reduced, mainly reflecting the gradual change from complete BITD (C_BITD) throughout the entire length of the binder yarn to occurring only in the middle of the curved portion of the binder yarn.
- (iv) WFLD almost does not change with the variation of M_F .

To investigate the reason, as the M_F increases, the inclination angle of the binder yarns increases, and the bundling effect between the binder yarns and weft yarns increases under weft-loading, which restricts the occurrence of BITD, allowing the strain energy transfer to the matrix and the warp yarns, which in turn improves the degree of MD and WPTD.

6.5 Progressive Damage Process Analysis

6.5.1 Damage Process under Warp-Loading

Figure 21 illustrates the propagation process of different damaged elements under warp-loading. Among them, Fig. 21(a and b) shows the comparison between the percentages of damaged elements and complete damaged elements of each component with different M_F at the failure stage. Figure 21(c-i) shows the specific propagation process of damaged elements of MD, WPLD, BILD, WFLD, WPTD, BITD, and WFTD with different M_F . In

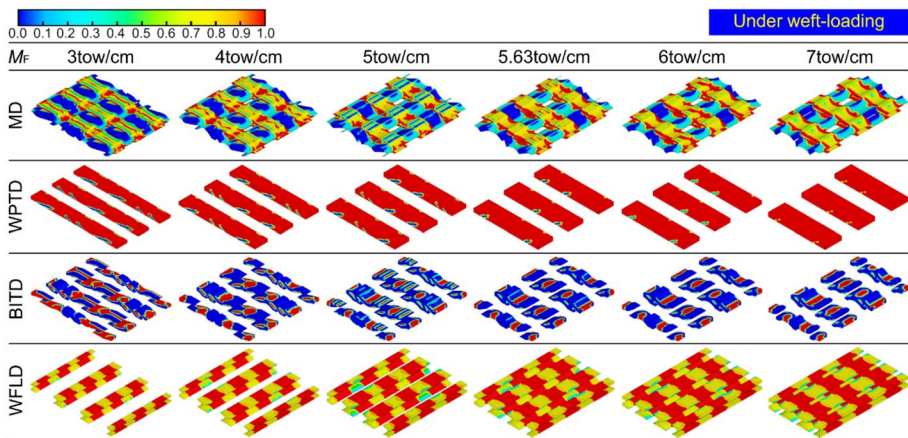


Fig. 20 Comparison of ultimate damage nephograms of various components with different weft yarn arrangement densities under weft-loading

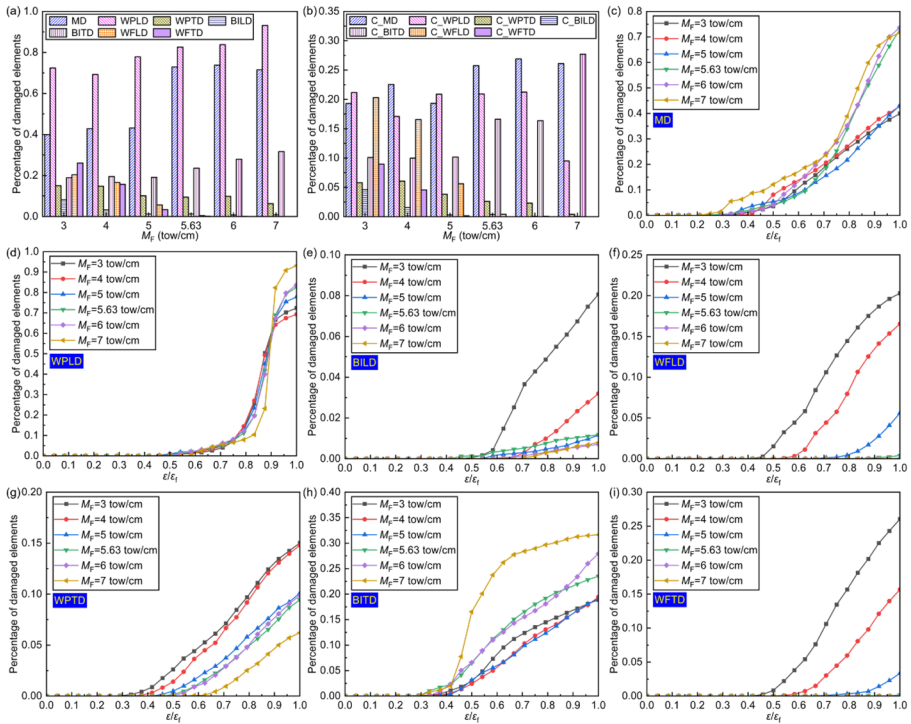


Fig. 21 Comparison of the percentage of different **a** damaged elements and **b** complete damaged elements with different weft yarn arrangement densities; relationship between the percentage of different damaged elements with the warp-loading process: **c** MD, **d** WPLD, **e** BILD, **f** WFLD, **g** WPTD, **h** BITD, and **i** WFTD

general, the extension curves of different damaged elements with different M_F show the trend of “slow-fast-slow”, which is consistent with the damage behavior of different components in the literature [53]. Nevertheless, there are still significant differences in the damage propagation process with different M_F .

As shown in Fig. 21(a and b), with the increase of M_F , both MD and C_MD show an increasing trend; WPLD shows an increasing trend, but C_WPLD does not show a significant trend; and the rest of the damage elements (WPTD, BILD, BITD, WFLD, and WFTD) and their corresponding complete damage elements (C_WPTD, C_BILD, C_BITD, C_WFLD, and C_WFTD) all show a decreasing trend. The reasons for these trends have been described above and will not be repeated here. Overall, the completely damaged elements are about 30% of the damaged elements, which is consistent with the results in the literature [53].

To further investigate the damage mechanism of 2.5D-THT-WR-WC under warp-loading, the propagation process of each damage mode with different M_F is specifically analyzed in the following:

- (i) From Fig. 21(c), it can be seen that when $\varepsilon/\varepsilon_t < 0.75$, the MD propagation process with different M_F is similar, and the overall propagation rate is small. After the period, the MD propagation with different M_F is divided into two parts, the first part is the MD

when $M_F > 5\text{tow/cm}$, which has a significantly higher propagation rate, and the second part is the MD when $M_F \leq 5\text{tow/cm}$, which almost has a constant propagation rate. The reason for this is that when the $M_F \leq 5\text{tow/cm}$, there is no contact between adjacent layers of binder yarns, and their inclination angle is smaller, which can share more loads, thus leading to no significant increase in the MD propagation rate. For similar reasons, the BITD (see Fig. 21(h)) also exhibits similar propagation patterns.

- (ii) From Fig. 21(d), it can be seen that the WPLD propagation with different M_F can be categorized into three stages. When $\varepsilon/\varepsilon_f < 0.75$, the relationship between M_F and damage propagation rate is basically irrelevant, and the overall propagation rate in this stage is low. When $0.75 < \varepsilon/\varepsilon_f < 0.9$, the larger M_F is, the slower the damage propagation is, and the overall propagation rate in this stage is rapidly increasing. When $\varepsilon/\varepsilon_f > 0.9$, the larger M_F is, the faster the damage propagation is, but the overall propagation rate in this stage is decreasing.
- (iii) From Fig. 21(e), it can be seen that the overall propagation rate of BILD decreases with the increase of M_F , which is mainly due to the difference in the inclination angle of the binder yarns resulting in their different load sharing. It is worth noting that the BILD propagation at $M_F = 5\text{tow/cm}$ is slightly slower than that at $M_F = 5.63\text{tow/cm}$, due to the fact that the adjacent layers of the binder yarns are touch each other when $M_F = 5.63\text{tow/cm}$, promoting the BILD propagation.
- (iv) From Fig. 21(f), it can be seen that the overall propagation rate of WFLD decreases with the increase of M_F , which is mainly due to the increase of load carried by the binder yarns at high MF, resulting in the increase of shear load on the weft yarns. For such reasons, similar propagation laws also exist for WPTD (see Fig. 21(g)) and WFTD (see Fig. 21(i)).

To further explore the damage positions and their propagation mechanisms of 2.5D-THT-WR-WC under warp-loading, the damage propagation process of different components when $M_F = 66\text{tow/cm}$ is presented in Fig. 22, which is analyzed as follows:

- (i) The initial MD positions are near the regions where the adjacent layers of the binder yarns are squeezed each other, and then the MD extends to the regions near the warp yarns on both sides. As loading continues, the MD of each part gradually forms a penetration until the C_MD connects into a whole region and the material fails.
- (ii) The initial WPLD appears in the part of the warp yarn close to the extruded area of the adjacent layers of the binder yarns, and then gradually extends to the inside of the warp yarn until the C_WPLD can penetrate into each other and the material loses its load-bearing capacity. The initial WPTD appears almost simultaneously with the WPLD, but the WPTD does not extend to the inside of the warp yarns, but only the damage degree increases at their edge region.
- (iii) The initial BILD appears at the curved-straight junctions of the binder yarn and does not extend to the interior of the binder yarn, besides an increase in the damage degree. The initial BITD appears at the extruded areas of the adjacent layers of the binder yarns, then the BITD also develops at their curved-straight junctions, and both parts of the BITD expand into the inner part of the binder yarns until the material fails.

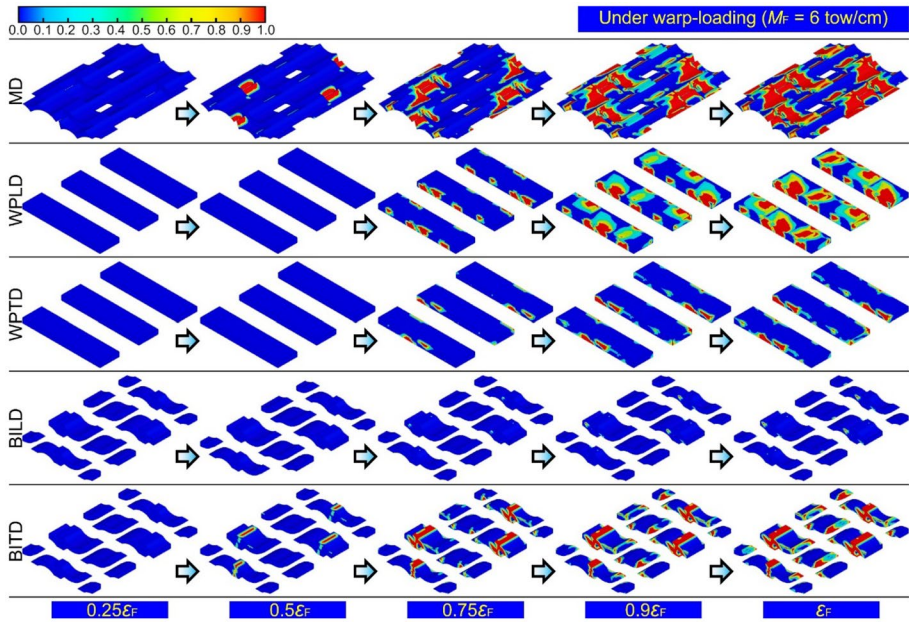


Fig. 22 Progressive damage propagation process of 2.5D-THT-WR-WC with $M_F=6$ tow/cm under warp-loading

Throughout the damage propagation process under warp-loading, the BITD and MD in its vicinity appear firstly due to the stress concentration at the extrusion areas of adjacent layers of the binder yarns, followed by the WPLD and WPTD. As loading proceeds, the WPLD extends to the interior of the warp yarns, with the incidental extension of the MD and the BITD, until the C_WPLD penetrates through the entire warp yarns, and the material failure occurs.

6.5.2 Damage Process under Weft-Loading

Figure 23 illustrates the propagation process of different damaged elements under weft-loading. Among them, Fig. 23(a and b) shows the comparison between the percentages of damaged elements and complete damaged elements of each component with different M_F at the failure stage. Figure 23(c-f) shows the specific propagation process of damaged elements of MD, WPTD, BITD, and WFLD with different M_F . In general, the expansion curves of each damaged element display a “slow-fast-slow” trend, which is similar to that under weft-loading.

As shown in Fig. 23(a and b), the percentage of MD, WPTD, C_WPTD, and WFLD is almost close to 100%; the percentage of C_MD and C_BITD increases and decreases with the increase of M_F , respectively; and the percentage of C_WFLD almost unchanged with the change of M_F . Obviously, the effect of M_F on the damage pattern under weft-loading is relatively small, and it is only the slightly different stress concentration effects produced by the binder yarns with different M_F that lead to a slight difference in the percentage of damage elements of each component. It should be noted that under weft-loading, the binder yarn is in transverse tension, while under warp-loading, the binder yarn is in longitudinal

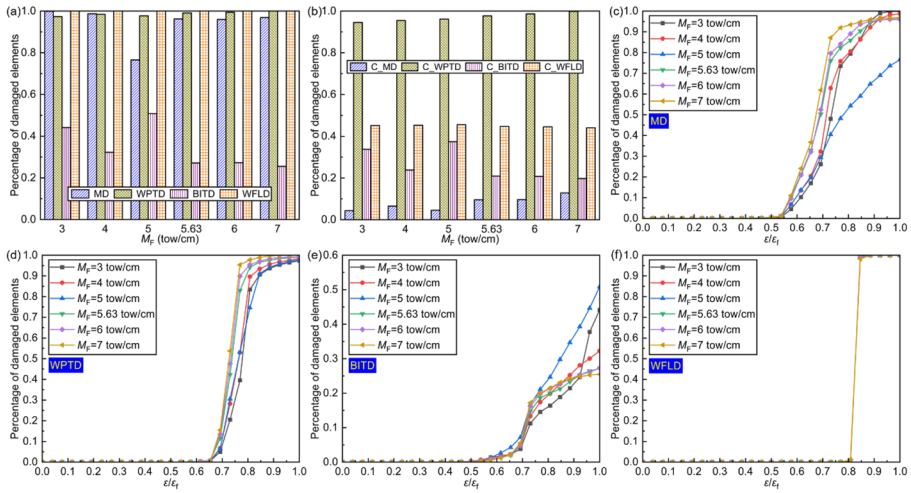


Fig. 23 Comparison of the percentage of different **a** damaged elements and **b** complete damaged elements with different weft yarn arrangement densities; relationship between the percentage of different damaged elements with the weft-loading process: **c** MD, **d** WPTD, **e** BITD, and **f** WFLD

tension, so the stress concentration effect produced by the binder yarn under weft-loading is much smaller than that under warp-loading.

To further investigate the damage mechanism of 2.5D-THT-WR-WC under weft-loading, the propagation process of each damage mode with different M_F is specifically analyzed in the following:

- (i) From Fig. 23(c), it can be seen that when $\epsilon/\epsilon_f=0.55$, MD at different M_F begin to sprout and propagate rapidly, in which the higher the M_F , the greater the overall damage propagation rate. It is worth noting that at $M_F=5$ tow/cm, the MD damage propagation rate is significantly smaller than that in other conditions because stress concentration effect of the binder yarns is more significant, resulting in the binder yarns absorbing most of the strain energy, thus making a weaker MD. When , the damage propagation rate of MD decreases until the material fails.
- (ii) From Fig. 23(d), it can be seen that when $\epsilon/\epsilon_f=0.65$, WPTD begins to sprout with different M_F , and the larger the M_F is, the larger the WPTD propagation rate is; when $\epsilon/\epsilon_f=0.8$, the WPTD damage propagation rate decreases until the material fails. During the whole process, the load on the warp yarns is similar to the transverse tension of unidirectional composites, so the contact area between the warp yarns and the binder yarns determines the WPTD propagation rate, and the larger the contact area is, the larger the WPTD propagation rate is.
- (iii) From Fig. 23(e), it can be seen that the BITD propagation shows a complementary trend with the MD propagation, which is mainly reflected in the fact that the BITD propagation rate when $M_F=5$ tow/cm is significantly higher than the other conditions, the reason for which has already been described above and will not be repeated here.
- (iv) From Fig. 23(f), it can be seen that the WFLD propagation rate is almost independent of the M_F , and when $\epsilon/\epsilon_f=0.8$, i.e. when the propagation rate of other damage modes

begins to slow down, the percentage of WFLD elements undergoes an explosion, which is characterized by brittle fracture.

To further explore the damage positions and their propagation mechanisms of 2.5D-THT-WR-WC under weft-loading, the damage propagation process of different components when $M_F = 6$ tow/cm is presented in Fig. 24, which is analyzed as follows:

- (i) The initial MD positions are mainly distributed at the boundary between the warp yarns and binder yarns, and then expand to the warp and weft directions simultaneously. As the loading continues, the damage degree increases until the C_MD forms a continuous region at the boundary until material failure occurs.
- (ii) The initial WPTD sprouts near the extrusion areas of the adjacent layers of the binder yarns, and then expands toward the interior of the warp yarns until the C_WPTD penetrates through the entire warp yarn cross-section. Subsequently, the WPTD continues to expand in the weft direction until the C_WPTD is connected throughout the entire warp yarns.
- (iii) The initial BITD also sprouts at the extrusion areas of the adjacent layers of the binder yarns, and then extends to the inner part of the binder yarns, but does not extend in the weft direction due to the constraining effect of the weft yarns.
- (iv) The WFLD propagation exhibits a global character, i.e. almost all elements of the weft yarn are damaged at the same time, and the damage degree increases simultaneously until the C_WFLD is penetrating through the entire weft yarns cross-section and the material loses its load-carrying capacity.

Throughout the damage propagation process under weft-loading, the WPTD and its neighboring regions of MD and BITD appear firstly due to the stress concentration at the extrusion areas of the adjacent layers of the binder yarns. As the loading continues, these three damage modes propagate until the weft yarns are difficult to carry alone, making the WFLD propagate rapidly and the material failure occurs.

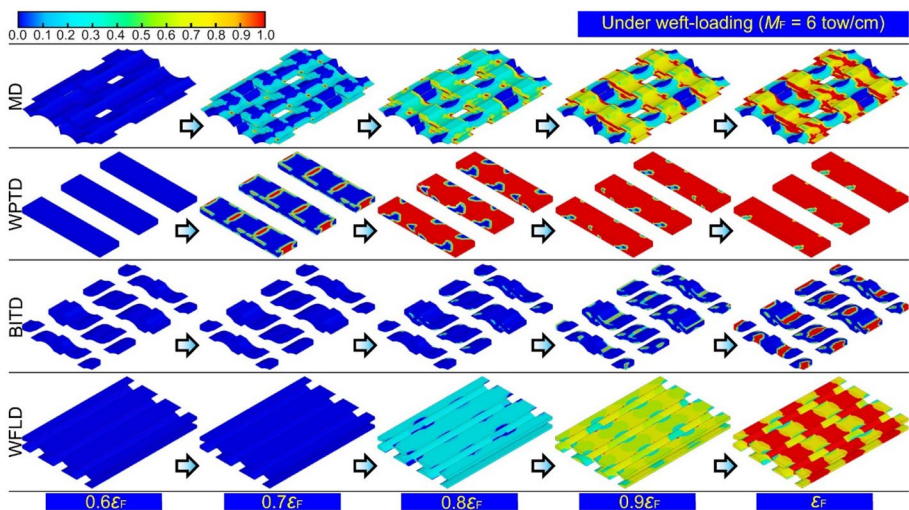


Fig. 24 Progressive damage propagation process of 2.5D-THT-WR-WC with $M_F = 6$ tow/cm under weft-loading

7 Conclusions

In this work, a new structure, 2.5D-THT-WR-WC, formed by the compounding of SCLS structure and SLS structure, is investigated. First, assumptions are made about different yarn cross-sections and orientations, and on this basis, a variety of geometric relationships for the yarn system of 2.5D-THT-WR-WC are discussed and expressions for the geometric relationships are derived. Subsequently, considering the effect of weft yarn arrangement density M_F on the mesoscopic structure of the yarn system, six unit-cell models with different mesoscopic features and their corresponding finite element models are established. Lastly, the mechanical properties and failure mechanism of the material are analyzed by combining the results of the warp/weft static-load experiments of the 2.5D-THT-WR-WC specimens, and the following results with engineering value are obtained:

- (i) Under either warp-loading or weft-loading, the maximum prediction errors for modulus and strength are 6.3% and 11.7%, respectively; there is good agreement between the predicted and experimental stress-strain curves, especially under weft-loading; the physical fracture is similar to the ultimate simulated damage morphology in many key features, such as the damage position and damage degree of the warp yarns and binder yarns. The consistency of these three comparisons demonstrates that the established unit-cell model combined with the developed progressive damage model can effectively predict the mechanical properties and failure behavior of 2.5D-THT-WR-WC.
- (ii) As M_F increases under warp-loading, both modulus and strength show a nonlinear decreasing trend with decreasing variation rate, the overall stress level decreases under the same load, and the nonlinearity of the stress-strain curves increases, which is mainly attributed to the changes in the inclination angle of the binder yarns and the changes in the extrusion effect between adjacent layers of the binder yarns.
- (iii) As M_F increases under weft-loading, both modulus and strength increase linearly, the overall stress level under the same load is almost constant, and the stress-strain curves show the similar change trend, which is mainly attributed to the changes in the volume percentage of the weft yarns and the weakening of the bundling effect of the binder yarns.
- (iv) In the warp-loading damage process, due to the stress concentration at the extrusion areas of adjacent layers of the binder yarns, BITD and MD in the nearby area appear firstly, and then WPLD and WPTD begin to sprout, as well as the propagation of WPLD into the interior of the warp yarns, with the incidental propagation of MD and BITD, until the C_WPLD penetrates through the entire warp yarns, the failure of the material occurs. Furthermore, as M_F increases, the damage degree of BITD increases, while that of other damage modes decreases, owing to the increase in the inclination angle of the binder yarn, which has a more obvious straightening effect during the loading process.
- (v) In the weft-loading damage process, since the stress concentration at the extrusion areas of adjacent layers of the binder yarns, BITD and its nearby region of WPTD and MD appear firstly, and then these three damage modes keep expanding until the weft yarns are difficult to carry alone, the WFLD propagates rapidly, and the material failure occurs. Moreover, as M_F increases, the damage degree of BITD decreases, while that of other damage modes increases, owing to the increase in the inclination angle of the binder yarn, which makes the bundling effect of the binder yarns with the weft yarns more significant.

In summary, the mechanical properties of 2.5D-THT-WR-WC are analyzed by constructing unit-cell models with different M_F in this work. It is worth noting that the constructed unit-cell model is only applicable to the resin-based materials formed using the RTM process, but is not limited to the type of fiber reinforcement. In future, with the increasing theoretical and engineering requirements, researchers can consider the changes occurring in the molding process of 2.5D-THT-WR-WC, such as surface extrusion deformation, internal porosity, etc., to establish a unit-cell model that is more consistent with the actual material, and thus predict the mechanical behavior more accurately, based on the present work.

Author Contributions Junhua Guo: Conceptualization, Methodology, Formal analysis, Writing-original draft; Gaofeng Zhou: Formal analysis, Writing-review & editing; Huabing Wen: Validation, Supervision; Hongjian Zhang: Supervision; Haitao Cui: Visualization; Weidong Wen: Supervision; Chun Guo: Conceptualization, Writing-review & editing; Yifan Zhang: Visualization, Supervision.

Funding This work has been supported by National Science and Technology Major Project (No. 2017-IV-0007-0044), National Natural Science Foundation of China (No. 52175142).

Declarations

Competing Interest The authors declare no competing interests.

References

- Zhang, Y., Tong, J., Guo, Q., Guo, J., Liu, X., Chen, L.: Hierarchical multiscale analysis for 3D woven composite leaf spring landing gear. *Thin. Wall. Struct.* **189**, 110913 (2023)
- Guo, J., Wen, W., Zhang, H., Cui, H.: A mesoscale fatigue progressive damage model for 3D woven composites. *Int. J. Fatigue.* **152**, 106455 (2021)
- Guo, J., Wen, W., Zhang, H., Cui, H.: Warp-loaded mechanical performance of 3D orthogonal layer-to-layer woven composite perforated structures with different apertures. *Compos. Struct.* **278**, 114720 (2021)
- Zhang, H., Guo, J., Wen, W., Cui, H., He, S., Xu, Y.: Bending/tensile tests and simulations of the 2.5D woven T-shaped hooking composite structure. *Compos. Struct.* **206**, 155–163 (2018)
- Wang, Y., Gong, Y., Zhang, Q., He, Y., Jiao, J., Hu, N.: Vibration fatigue properties of laminated and 2.5D woven composites: a comparative study. *Int. J. Fatigue.* **168**, 107466 (2023)
- Ma, Z., Zhang, P., Zhu, J.: Review on the fatigue properties of 3D woven fiber/epoxy composites: testing and modelling strategies. *J. Ind. Text.* **51**(5_suppl), 7755S–7795S (2022)
- Guo, L., Huang, J., Zhang, L., Sun, X.: Damage evolution of 3D woven carbon/epoxy composites under tension-tension fatigue loading based on synchrotron radiation computed tomography (SRCT). *Int. J. Fatigue.* **142**, 105913 (2021)
- Li, D., Dang, M., Jiang, L.: Elevated temperature effect on tension fatigue behavior and failure mechanism of carbon/epoxy 3D angle-interlock woven composites. *Compos. Struct.* **268**, 113897 (2021)
- Guo, L., Liao, F., Xu, Y., Wang, T., Yang, C., Yuan, J.: Experimental method and failure mechanisms investigation for out-of-plane shear fatigue behavior of 3D woven composites. *Int. J. Fatigue.* **134**, 105501 (2020)
- Saboktakin, A.: 3D textile preforms and composites for aircraft structures: a review. *Int. J. Aviat. Aeronaut.* **6**(1), 2 (2019)
- Rubino, F., Nisticò, A., Tucci, F., Carlone, P.: Marine application of fiber reinforced composites: a review. *J. Mar. Sci. Eng.* **8**(1), 26 (2020)
- Guo, J., Wen, W., Zhang, H., Cui, H., Song, J.: Representative cell modeling strategy of 2.5D woven composites considering the randomness of weft cross-section for mechanical properties prediction. *Eng. Fract. Mech.* **237**, 107255 (2020)

13. Song, J., Wen, W., Cui, H., Li, L.: Weft direction tension-tension fatigue responses of layer-to-layer 3D angle-interlock woven composites at room and elevated temperatures. *Int. J. Fatigue*. **139**, 105770 (2020)
14. Song, J., Wen, W., Cui, H., Wang, Y., Lu, Y., Long, W., et al.: Warp direction fatigue behavior and damage mechanisms of centrally notched 2.5D woven composites at room and elevated temperatures. *Compos. Sci. Technol.* **182**, 107769 (2019)
15. Song, J., Wen, W., Cui, H.: Experimental and numerical investigation of mechanical behaviors of 2.5D woven composites at ambient and un-ambient temperatures. *Compos. Struct.* **201**, 699–720 (2018)
16. Song, J., Wen, W., Cui, H.: Fatigue life prediction model of 2.5D woven composites at various temperatures. *Chinese. J. Aeronaut.* **31**(2), 310–329 (2018)
17. Song, J., Wen, W., Cui, H.: Fatigue behaviors of 2.5D woven composites at ambient and un-ambient temperatures. *Compos. Struct.* **166**, 77–86 (2017)
18. Song, J., Zhang, Y., Guo, X.: Thermomechanical fatigue behaviors and failure mechanism of 2.5D shallow curve-link-shaped woven composites. *Compos. Struct.* **284**, 115080 (2022)
19. Zhao, Y., Song, J., Wen, W., Cui, H., Li, C., Liu, S.: Thermo-mechanical behaviors of 2.5D shallow straight-link-shaped woven composites under the warp direction fatigue loading at room and elevated temperatures. *Compos. Struct.* **289**, 115489 (2022)
20. Verpoest, I., Lomov, S.: Virtual textile composites software: integration with micro-mechanical, permeability and structural analysis. *Compos. Sci. Technol.* **65**(15–16), 2563–2574 (2005)
21. Gereke, T., Cherif, C.: A review of numerical models for 3D woven composite reinforcements. *Compos. Struct.* **209**, 60–66 (2019)
22. Isart, N., Mayugo, J.A., Blanco, N., Ripoll, L., Solà, A., Soler, M.: Geometric model for 3D through-thickness orthogonal interlock composites. *Compos. Struct.* **119**, 787–798 (2015)
23. Zhou, Y., Wen, W., Cui, H.: Spatial modelling of 3D woven variable thickness composite plate at the mesoscopic scale. *Compos. Struct.* **239**, 111946 (2020)
24. Zhang, X., Zhang, S., Jia, Y., Liu, C., Gao, X., Wang, F., et al.: A parameterized and automated modelling method for 3D orthogonal woven composite RVEs considering yarn geometry variations. *Compos. Struct.* **305**, 116496 (2023)
25. Stig, F., Hallström, S.: A modelling framework for composites containing 3D reinforcement. *Compos. Struct.* **94**(9), 2895–2901 (2012)
26. Mahadik, Y., Hallett, S.R.: Finite element modelling of tow geometry in 3D woven fabrics. *Compos. Part A-Appl S.* **41**(9), 1192–1200 (2010)
27. El Said, B., Green, S., Hallett, S.R.: Kinematic modelling of 3D woven fabric deformation for structural scale features. *Compos. Part. A-Appl. S.* **57**, 95–107 (2014)
28. Green, S.D., Long, A.C., El Said, B.S.F., Hallett, S.R.: Numerical modelling of 3D woven preform deformations. *Compos. Struct.* **108**, 747–756 (2014)
29. Jia, Y., Yu, G., Du, J., Gao, X., Song, Y., Wang, F.: Adopting traditional image algorithms and deep learning to build the finite model of a 2.5D composite based on X-ray computed tomography. *Compos. Struct.* **275**, 114440 (2021)
30. Naouar, N., Vidal-Sallé, E., Schneider, J., Maire, E., Boisse, P.: Meso-scale FE analyses of textile composite reinforcement deformation based on X-ray computed tomography. *Compos. Struct.* **116**, 165–176 (2014)
31. Naouar, N., Vidal-Salle, E., Schneider, J., Maire, E., Boisse, P.: 3D composite reinforcement meso F.E. Analyses based on X-ray computed tomography. *Compos. Struct.* **132**, 1094–1104 (2015)
32. Guo, C., Zhang, H., Wang, Y., Jia, Y., Qi, L., Zhu, Y., et al.: Parametric modeling of 2.5D woven composites based on computer vision feature extraction. *Compos. Struct.* **321**, 117234 (2023)
33. Hallal, A., Younes, R., Fardoun, F., Nehme, S.: Improved analytical model to predict the effective elastic properties of 2.5D interlock woven fabrics composite. *Compos. Struct.* **94**(10), 3009–3028 (2012)
34. Tan, P., Tong, L., Steven, G.P.: Micromechanics models for mechanical and thermomechanical properties of 3D through-the-thickness angle interlock woven composites. *Compos. Part. A-Appl. S.* **30**(5), 637–648 (1999)
35. Byun, J.H., Chou, T.W.: Elastic properties of three-dimensional angle-interlock fabric preforms. *J. Text. I.* **81**(4), 538–548 (1990)
36. Pochiraju, K., Chou, T.: Three-dimensionally woven and braided composites. I. A model for anisotropic stiffness prediction. *Polym. Compos.* **20**(4), 565–580 (1999)
37. Fang, G., Liang, J., Lu, Q., Wang, B., Wang, Y.: Investigation on the compressive properties of the three dimensional four-directional braided composites. *Compos. Struct.* **93**(2), 392–405 (2011)
38. Lu, H., Guo, L., Liu, G., Zhang, L.: A progressive damage model for 3D woven composites under compression. *Int. J. Damage. Mech.* **28**(6), 857–876 (2019)

39. Zhong, S., Guo, L., Liu, G., Lu, H., Zeng, T.: A continuum damage model for three-dimensional woven composites and finite element implementation. *Compos. Struct.* **128**, 1–9 (2015)
40. Zixing, L., Zhou, Y., Yang, Z., Liu, Q.: Multi-scale finite element analysis of 2.5D woven fabric composites under on-axis and off-axis tension. *Comput. Mater. Sci.* **79**, 485–494 (2013)
41. Li, D., Dang, M., Jiang, L.: Fatigue behavior and failure mechanisms of 3D angle-interlock woven composite at room and cryogenic temperatures under bending. *Compos. Commun.* **23**, 100559 (2021)
42. Liu, X., Wang, X., Zhang, D., Qian, K.: Effect of voids on fatigue damage propagation in 3D5D braided composites revealed via automated algorithms using X-ray computed tomography. *Int. J. Fatigue.* **158**, 106778 (2022)
43. Liu, X., Zhang, D., Mao, C., Wang, X., Qian, K.: Full-field progressive fatigue damage of 3D5D braided composites with yarn-reduction: visualization, classification, and quantification. *Compos. Sci. Technol.* **218**, 109214 (2022)
44. Liu, X., Zhang, D., Qiu, H., Sun, J., Mao, C., Qian, K.: On-axis fatigue behaviors and failure characterization of 3D5D braided composites with yarn-reduction using X-ray computed tomography. *Compos. Sci. Technol.* **203**, 108585 (2021)
45. Zhang, Y., Guo, Q., Chen, X., Xie, J., Chen, L.: Effect of apertures on tensile property of warp-reinforced 2.5D woven composites notched plates. *Compos. Struct.* **252**, 112693 (2020)
46. Guo, L., Liao, F., Li, Z., Huang, J., Zhao, J., Zheng, T.: Research progress in damage evolution of woven composites. *Sci. Sin. Tech.* **252**, 876–896 (2020)
47. Li, S.: Research of Mechanical Properties and Strength Failure Criteria of Component Materials under Temperature Environment. Nanjing University of Aeronautics and Astronautics (2020)
48. Hashin, Z.: Failure criteria for unidirectional Fiber composites. *J. Appl. Mech.* **47**, 329–334 (1980)
49. Guo, J., Zhang, Y., Zhou, G., Wen, H., Wen, W., Zhang, H., et al.: A transverse failure criterion for unidirectional composites based on the Puck failure surface theory. *Compos. Sci. Technol.* **242**, 110192 (2023)
50. Wiegand, J., Petrinic, N., Elliott, B.: An algorithm for determination of the fracture angle for the three-dimensional Puck matrix failure criterion for UD composites. *Compos. Sci. Technol.* **68**(12), 2511–2517 (2008)
51. Guo, J., Wen, W., Zhang, H., Cui, H., Song, J., Liu, H.: Investigation of mechanical properties for 2.5D woven composites with different weft-layer-numbers by a triple-cell model system. *J. Ind. Text.* **51**(3_suppl), 5243S–5285S (2022)
52. Yang, H.: Research on the Strength of Three-Piece Warp-Lined 2.5D Woven Composite Material under Temperature Environment. Nanjing University of Aeronautics and Astronautics (2021)
53. Guo, J., Wen, W., Zhang, H., Cui, H.: Influence of notch shape on the quasi-static tensile behavior of 2.5D woven composite structure. *Thin. Wall. Struct.* **165**, 107944 (2021)
54. Lomov, S.V., Bogdanovich, A.E., Ivanov, D.S., Mungalov, D., Karahan, M., Verpoest, A.: A comparative study of tensile properties of non-crimp 3D orthogonal weave and multi-layer plain weave E-glass composites. Part 1: materials, methods and principal results. *Compos. Part. A-Appl. S.* **40**, 1134–1143 (2009)
55. Ivanov, D.S., Lomov, S.V., Bogdanovich, A.E., Karahan, M., Verpoest, I.: A comparative study of tensile properties of non-crimp 3D orthogonal weave and multi-layer plain weave E-glass composites. Part 2: comprehensive experimental results. *Compos. Part. A-Appl. S.* **40**, 1144–1157 (2009)
56. Jabbar, M., Nawab, Y., Karahan, M., Ashraf, M., Hussain, T.: Mechanical response of novel 3D woven flax composites with variation in z yarn binding. *J. Nat. Fibers.* **17**(6), 890–905 (2020)
57. Jabbar, M., Shaker, K., Nawab, Y., Umair, M.: Effect of the stuffer yarns on the mechanical performance of novel 3D woven green composites. *Compos. Struct.* **269**, 114023 (2021)
58. Karahan, M., Lomov, S.V., Bogdanovich, A.E., Mungalov, D.M., Verpoest, I.: Internal geometry evaluation of non-crimp 3D orthogonal woven carbon fabric composite. *Compos. Part. A-Appl. S.* **41**, 1301–1311 (2010)

Publisher's Note Springer Nature remains neutral with regard to jurisdictional claims in published maps and institutional affiliations.

Springer Nature or its licensor (e.g. a society or other partner) holds exclusive rights to this article under a publishing agreement with the author(s) or other rightsholder(s); author self-archiving of the accepted manuscript version of this article is solely governed by the terms of such publishing agreement and applicable law.